

Adaptive finite difference methods for the Willmore flow: mesh redistribution algorithm and tangential velocity approach

Zhenghua Duan^a, Meng Li^{*a}

^a*School of Mathematics and Statistics, Zhengzhou University, Zhengzhou 450001, China*

Abstract

We develop two adaptive finite difference methods for the numerical simulation of the Willmore flow, employing the k th-order backward differentiation formula (BDF k) for time discretization, together with monitor functions for dynamic mesh adaptation along evolving interfaces. The first approach is based on a weighted arc-length equidistribution strategy driven by a monitor function to adaptively redistribute grid points. An adaptive monitor selection mechanism, constructed from the curvature and its variation, enhances spatial resolution in regions of strong geometric complexity while preserving mesh regularity. The second approach eliminates explicit reparameterization by incorporating a tangential velocity into the Willmore flow, with mesh redistribution inherently embedded in the geometric evolution. We further develop an energy-stable correction algorithm for the second method to guarantee discrete energy stability at the theoretical level. In both approaches, the monitor function serves as the core component of the adaptive framework, encoding essential geometric information—such as curvature and curvature variation—to guide mesh refinement and redistribution. Extensive numerical experiments demonstrate that the proposed BDF k -based adaptive schemes accurately capture the geometric evolution of the Willmore flow and exhibit excellent robustness and computational efficiency for problems involving complex interface geometries.

Keywords: Willmore flow; weighted equidistribution principle; mesh redistribution algorithm; adaptive tangential velocity; monitor function

1. Introduction

Interface bending in flexible membranes and other soft interfacial systems generates curvature-dependent elastic energy [1], which subsequently drives the interface toward smoother and mechanically more stable configurations [2–5]. Examples arise in cell membranes, biological vesicles [6], thin film [7, 8], and nanoscale structures, where the interfacial morphology is often governed by an underlying energy-minimization principle [9–11]. To provide a mathematical description of such curvature-dominated relaxation processes, Willmore introduced a curvature-based bending energy model in his study of closed surface geometry. This energy functional has since been widely adopted for analyzing the morphological evolution of elastic interfaces.

The Willmore flow is precisely the L^2 -gradient flow of this bending energy [12, 13], and its evolution is driven by the tendency to reduce the total curvature-dependent elastic energy. For a planar curve Γ , the Willmore energy is typically defined as [14]

$$W(\Gamma) = \frac{1}{2} \int_{\Gamma} \kappa^2 ds, \quad (1.1)$$

where κ denotes the curvature and ds is the element of arclength. The resulting gradient flow can be interpreted as a curvature-diffusion mechanism: regions of high curvature relax rapidly, whereas low-curvature regions evolve more slowly, guiding the interface toward a smoother and energetically minimized equilibrium configuration. As a higher-order generalization of the mean curvature flow, the Willmore flow plays an important role not only in differential geometry [15, 16] but also in applications such as thin-film relaxation in materials science [7, 8], membrane stability in biophysics [4, 6], and curve or surface fairing in computational geometry and image processing [17–19].

Building on the energetic formulation, the evolution of a planar curve under the Willmore flow is governed by a fourth-order geometric partial differential equation. More precisely, letting $\mathbf{X}(s, t)$ denote a parametrization of $\Gamma(t)$, the normal velocity of the curve is given by [20]

$$\partial_t \mathbf{X} \cdot \mathbf{n} = V, \quad V = \partial_{ss} \kappa + \frac{1}{2} \kappa^3,$$

Email address: This author's research was supported by National Natural Science Foundation of China (Nos. 11801527, U23A2065). Corresponding author: limeng@zzu.edu.cn. (Meng Li^{*})

where V is the normal velocity and ∂_s denotes differentiation with respect to arclength. In this formulation, the Willmore flow appears as a curvature-diffusion process, with the normal velocity governed by a differential operator involving the second derivative of κ .

The Willmore flow features a complex geometric structure and involves higher-order derivatives, which substantially increases the difficulty of numerical simulation. At the same time, ensuring that numerical simulations can maintain stability, accuracy, and high-quality mesh distribution throughout intricate geometric evolutions has also become a key issue in its numerical study. Rusu [21] formulated a mixed weak problem by introducing the mean curvature vector as an additional unknown, and on this basis constructed a finite element discretization for the evolution. In [22], Barrett et al. proposed a parametric finite element method (PFEM) framework suitable for the Willmore flow and other fourth-order geometric evolution equations. Kovács, Li, and Lubich [23] rigorously established convergence of higher-order surface finite element discretizations for the Willmore flow. Bao et al. [24] developed a fully discretized PFEM for the planar Willmore flow and proved its unconditional energy stability based on two newly derived geometric identities. Li and Li [25] established an energy-stable parametric finite element approximation for the generalized axisymmetric Willmore flow with closed surfaces. Garcke et al. [26] proposed stable finite element schemes for the planar Willmore flow and proved unconditional energy stability of their fully discrete methods.

While PFEMs are widely successful for curvature-driven surface evolution, they may also suffer from mesh degradation, including node accumulation or distortion, especially in long-time evolution or when the interface undergoes strong curvature variations or rapid shape changes. In such cases, mesh redistribution strategies are beneficial for maintaining mesh quality and numerical stability. In [27], Bänsch et al. developed a variational finite element framework for fourth-order geometric flows and incorporated mesh regularization together with temporal and spatial adaptivity to prevent mesh distortion, thereby improving mesh quality in simulations of the Willmore flow. Steinhilber developed discrete harmonic map algorithms and used them to construct a reparametrization strategy for geometric evolution equations. Applied to the Willmore flow, this approach effectively improves mesh quality during the evolution [28]. Barrett, Garcke, and Nürnberg proposed a parametric finite element formulation (commonly referred to as the BGN method) that does not require any explicit mesh redistribution procedure or remeshing; instead, the weak formulation intrinsically generates a favorable tangential velocity that drives the mesh nodes toward a naturally equidistributed configuration along the curve, thereby preventing mesh distortion during the evolution in [22, 29, 30]. Besides the BGN method, Elliott and Fritz proposed a reparametrization approach based on special solutions of the harmonic map heat flow (an idea inspired by the DeTurck trick) which introduces an intrinsic tangential motion that yields a more uniform redistribution of mesh points and thereby improves mesh quality during geometric evolutions [31]. The above methods have demonstrated good effectiveness in improving mesh quality and have been applied to a wide range of geometric flows. Nevertheless, in certain situations, they may still suffer from simulation breakdowns, especially when the evolving interface involves extremely large curvature or highly localized and rapidly varying curvature.

In addition, a broad class of moving mesh methods founded on adaptive mesh redistribution has been developed [32–34], which enables more direct and systematic control over the distribution of mesh points throughout the evolution process. Huang et al. [34] investigated a family of moving mesh partial differential equations derived from the equidistribution principle, providing stability analysis, demonstrating the absence of mesh crossing under weak assumptions, and evaluating their performance through numerical tests. Li et al. [35] proposed an adaptive moving mesh framework that incorporates the concept of harmonic maps, in which mesh redistribution is carried out by iteratively constructing a harmonic mapping between the physical and parameter spaces, thereby generating high-quality meshes without changing the number of nodes. Mackenzie et al. [36] further developed an adaptive moving mesh method for the forced mean curvature flow, in which the tangential velocity is determined automatically from an equidistribution principle, enabling effective node concentration in regions of high curvature. Nevertheless, for more complex higher-order geometric flows such as the Willmore flow, no adaptive moving mesh methods have been developed, and there is a clear need for mesh redistribution strategies that can handle the higher-order nature of the evolution, maintain mesh quality under strong curvature variations, and remain robust in long-time simulations. These considerations constitute the main focus of the present work.

The main contributions of this work are summarized as follows:

- Based on the k th-order backward differentiation formula (BDFk) method in time and second-order centered finite differences in space, we construct a family of finite difference methods (FDMs) for the Willmore flow, referred to as BDFk-FDMs. For nearly convex or mildly perturbed curves with smooth geometric variation, these methods yield asymptotically equidistributed meshes (see Fig. 2.1). However, when the curve exhibits more intricate geometric features or undergoes rapid curvature changes, the mesh quality deteriorates significantly and may even cause a breakdown of the evolution (see Fig. 2.2).
- To overcome the above limitations, we develop an adaptive mesh redistribution strategy for the Willmore flow, termed the adaptive weighted arc-length redistribution (A-WAR) algorithm. The method is based on a monitor function that incorporates the curvature, its arc-length derivative, and the squared curvature. Based on a detailed

error analysis (see Appendix A), we establish the necessity of such adaptive monitoring strategies, and one of the key innovations of the A-WAR algorithm lies in its capability to adaptively select suitable monitor functions according to the local geometric properties of the discrete curve. Numerical experiments demonstrate that the A-WAR algorithm effectively eliminates the mesh deterioration observed in BDFk-FDMs and consistently produces high-quality meshes, even in the presence of large curvature or rapid curvature variations (see the comparisons between Fig. 2.2 and Fig. 3.1).

- By combining the tangential velocity equation, derived from the variational derivative of a mesh functional associated with a chosen monitor function, with the normal velocity equation, we obtain a new total velocity formulation, which leads to a fully adaptive moving mesh system for the Willmore flow. This formulation enables the construction of adaptive BDFk-FDMs (A-BDFk-FDMs) for the numerical solution of the resulting adaptive system. Building upon these schemes, we further introduce an energy-stable correction (EC) algorithm to guarantee the energy stability of the fully discrete method. Numerical experiments demonstrate that the overall adaptive framework, together with the EC algorithm, delivers accurate, stable, and efficient simulations across a wide range of challenging scenarios. In this set of numerical experiments, the monitor function used in the A-BDFk-FDMs can be chosen as a fixed function in advance, or selected adaptively according to the behavior of the discrete solution, following the A-WAR algorithm.

The remainder of the paper is organized as follows. In Section 2, we recall the parametric formulation of the planar Willmore flow and develop a family of finite difference schemes based on BDFk time discretizations. The mesh properties and limitations of the resulting BDFk-FDMs are also discussed. In Section 3, the A-WAR algorithm is introduced to dynamically improve mesh quality through a curvature-based monitor function. Section 4 presents a fully adaptive moving mesh formulation by coupling a tangential velocity equation with the Willmore flow, leading to the adaptive BDFk-FDMs; an EC algorithm is further developed to ensure discrete energy stability. Numerical experiments validating the accuracy, robustness, and efficiency of the proposed methods are presented in Section 5. Finally, conclusions and future research directions are given in Section 6. In Appendix A, we present a geometric rationale for the form of the monitor functions employed in this work, based on an analysis of the local interpolation error arising from approximating a smooth curve by a piecewise linear polygonal interpolant.

2. BDFk-FDMs

In this section, we first recall the classical continuous formulation of the Willmore flow. Then, we develop the FDMs for the Willmore flow, based on temporal BDFk discretizations.

2.1. Continuous formulation

Let $\Gamma(t) \subset \mathbb{R}^2$ denote a time-dependent smooth planar curve. Throughout the evolution, we represent $\Gamma(t)$ by a parametrized map

$$\mathbf{X}(\cdot, t) : \mathbb{T} \rightarrow \mathbb{R}^2, \quad \rho \mapsto \mathbf{X}(\rho, t) = (x(\rho, t), y(\rho, t))^T,$$

where $\mathbb{T} := \mathbb{R}/\mathbb{Z} = [0, 1]$ is the periodic reference domain. The initial curve is parametrized by $\mathbf{X}(\cdot, 0) = \mathbf{X}^0(\cdot)$. Based on this parametrization, the arc-length coordinate is introduced as $s(\rho, t) = \int_0^\rho |\partial_q \mathbf{X}(q, t)| dq$. With this definition, differentiation with respect to arc length is written as $\partial_s = \frac{1}{|\partial_\rho \mathbf{X}|} \partial_\rho$, and the corresponding arc-length element becomes $ds = |\partial_\rho \mathbf{X}| d\rho$. In addition, the tangent and normal vectors associated with the curve $\Gamma(t)$ are defined as follows

$$\boldsymbol{\tau} := \boldsymbol{\tau}(\rho, t) = \partial_s \mathbf{X}(\rho, t) = \frac{\partial_\rho \mathbf{X}(\rho, t)}{|\partial_\rho \mathbf{X}(\rho, t)|}, \quad \mathbf{n} := \mathbf{n}(\rho, t) = -\boldsymbol{\tau}^\perp, \quad (2.1)$$

where \perp denotes the clockwise rotation by $\frac{\pi}{2}$.

Then, the Willmore flow can be written as the following fourth-order geometric system. Given $\mathbf{X}(\rho, 0) = \mathbf{X}^0(\rho)$, we find $(\mathbf{X}(\rho, t), V(\rho, t), \kappa(\rho, t))$, $(\rho, t) \in \mathbb{T} \times (0, +\infty)$, such that

$$\partial_t \mathbf{X} \cdot \mathbf{n} = V, \quad (2.2a)$$

$$V = \partial_{ss} \kappa + \frac{1}{2} \kappa^3 = \frac{\partial_{\rho\rho} \kappa}{|\partial_\rho \mathbf{X}|^2} - \frac{\partial_\rho \kappa \partial_\rho \mathbf{X} \cdot \partial_{\rho\rho} \mathbf{X}}{|\partial_\rho \mathbf{X}|^4} + \frac{1}{2} \kappa^3, \quad (2.2b)$$

$$\kappa \mathbf{n} = -\partial_{ss} \mathbf{X} = -\frac{\partial_{\rho\rho} \mathbf{X}}{|\partial_\rho \mathbf{X}|^2} + \frac{\boldsymbol{\tau} \cdot \partial_{\rho\rho} \mathbf{X}}{|\partial_\rho \mathbf{X}|^3} \partial_\rho \mathbf{X}. \quad (2.2c)$$

Remark 1. Since the continuous formulation (2.2) coincides with that of the BGN framework, the resulting FDMs naturally yield approximately equidistributed meshes. The sole distinction between the present work and the classical BGN methods lies in the adoption of FDMs rather than FEMs. In the next subsection, we construct the corresponding FDMs and examine their mesh-preserving properties through simple numerical experiments. We also discuss several issues that may arise in more complex settings.

2.2. Finite difference discretizations

In this subsection, we present several finite difference discretizations of the Willmore flow (2.2). Let $h := \frac{1}{M}$ and $\Delta t := \frac{T}{N}$ denote the spatial grid size and the time step, where $M, N \in \mathbb{N}$. We introduce the uniform spatial partition $\rho_i := ih$, for $i = 0, 1, \dots, M-1$, with the periodicity condition $\rho_M \equiv \rho_0$, and the temporal grid $t^n := n\Delta t$, $n = 0, 1, 2, \dots, N$. The discrete curve at time t^n is then given by the nodal positions \mathbf{X}_i^n , which approximate $\mathbf{X}(\rho_i, t^n) \in \mathbb{R}^2$, for $i = 0, 1, \dots, M-1$ and $n = 0, 1, 2, \dots, N$.

To prepare the finite difference discretizations, we introduce the discrete derivative operators along the periodic parameter ρ . Let $f(\rho)$ denote a scalar- or vector-valued function sampled at the uniform grid points ρ_i with periodicity $f(\rho_{i+M}) = f(\rho_i)$. The forward, backward, centered first-order differences, together with the standard centered second-order difference used for curvature and other higher-order geometric quantities, are given by

$$\begin{aligned}\delta_\rho^+ f(\rho_i) &= \frac{f(\rho_i + h) - f(\rho_i)}{h}, & \delta_\rho^- f(\rho_i) &= \frac{f(\rho_i) - f(\rho_i - h)}{h}, \\ \delta_\rho f(\rho_i) &= \frac{f(\rho_i + h) - f(\rho_i - h)}{2h}, & \delta_{\rho\rho} f(\rho_i) &= \frac{f(\rho_i + h) - 2f(\rho_i) + f(\rho_i - h)}{h^2},\end{aligned}$$

where periodic extension is assumed, and all operators act componentwise when f is vector-valued. In the discrete settings, all geometric quantities introduced in Section 2.1 are approximated using finite difference operators along the periodic parameter ρ . In particular, the discrete tangent derivative is defined by the centered difference

$$\delta_\rho \mathbf{X}_i^n := \frac{\mathbf{X}_{i+1}^n - \mathbf{X}_{i-1}^n}{2h} \approx \partial_\rho \mathbf{X}(\rho_i, t^n),$$

and then the unit tangent and normal vectors are defined by

$$\boldsymbol{\tau}_i^n := \frac{\delta_\rho \mathbf{X}_i^n}{|\delta_\rho \mathbf{X}_i^n|}, \quad \mathbf{n}_i^n := R \boldsymbol{\tau}_i^n, \quad R = \begin{pmatrix} 0 & -1 \\ 1 & 0 \end{pmatrix}.$$

We discretize the spatial derivatives using second-order centered finite differences, and approximate the temporal derivative by using the BDFk method. Since the BDFk method requires the solution values from the previous $k-1$ time levels, the time integration is initialized by lower-order BDF schemes. Combining these approximations yields a family of BDFk finite-difference schemes for the parametric Willmore flow (2.2), hereafter referred to as the BDFk-FDMs. For given $\{(\mathbf{X}_i^{n-p}, V_i^{n-p}, \kappa_i^{n-p})\}_{p=0}^{k-1}$, the BDFk-FDM seeks the updated solution $(\mathbf{X}_i^{n+1}, V_i^{n+1}, \kappa_i^{n+1})$, such that

$$\frac{\sum_{p=0}^k \alpha_p \mathbf{X}_i^{n+1-p}}{\Delta t} \cdot \mathbf{n}_i^{n+1} = V_i^{n+1}, \quad (2.3a)$$

$$V_i^{n+1} = \frac{\delta_\rho \kappa_i^{n+1}}{|\delta_\rho \mathbf{X}_i^{n+1}|^2} - \frac{\delta_\rho \kappa_i^{n+1} \delta_\rho \mathbf{X}_i^{n+1} \cdot \delta_{\rho\rho} \mathbf{X}_i^{n+1}}{|\delta_\rho \mathbf{X}_i^{n+1}|^4} + \frac{1}{2} (\kappa_i^{n+1})^3, \quad (2.3b)$$

$$\kappa_i^{n+1} \mathbf{n}_i^{n+1} = -\frac{\delta_{\rho\rho} \mathbf{X}_i^{n+1}}{|\delta_\rho \mathbf{X}_i^{n+1}|^2} + \frac{\boldsymbol{\tau}_i^{n+1} \cdot \delta_{\rho\rho} \mathbf{X}_i^{n+1}}{|\delta_\rho \mathbf{X}_i^{n+1}|^3} \delta_\rho \mathbf{X}_i^{n+1}, \quad (2.3c)$$

where the coefficients $\{\alpha_p\}_{p=0}^k$ correspond to the k -step BDFk method. For instance, the coefficients of several commonly used BDFk methods are denoted by

$$\begin{aligned}\text{BDF1 } (k=1) : \quad & \alpha_0 = 1, \quad \alpha_1 = -1; \\ \text{BDF2 } (k=2) : \quad & \alpha_0 = \frac{3}{2}, \quad \alpha_1 = -2, \quad \alpha_2 = \frac{1}{2}; \\ \text{BDF3 } (k=3) : \quad & \alpha_0 = \frac{11}{6}, \quad \alpha_1 = -3, \quad \alpha_2 = \frac{3}{2}, \quad \alpha_3 = -\frac{1}{3}; \\ \text{BDF4 } (k=4) : \quad & \alpha_0 = \frac{25}{12}, \quad \alpha_1 = -4, \quad \alpha_2 = 3, \quad \alpha_3 = -\frac{4}{3}, \quad \alpha_4 = \frac{1}{4}.\end{aligned}$$

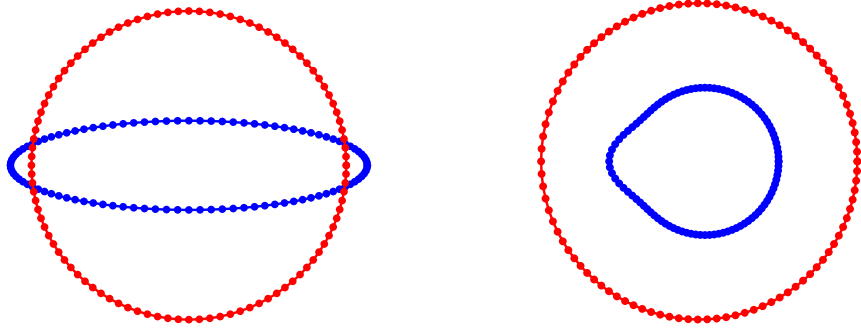


Figure 2.1: Representative examples showing well-maintained mesh quality. Blue curves represent the initial curves, and red curves represent the evolved curves at the final time. Left: the initial curves are given by $x = 4 \cos(2\pi\rho)$, $y = \sin(2\pi\rho)$, simulated with $k = 1$, $M = 100$, $T = 50$, $\Delta t = 0.01$. Right: the initial curves are given by $x = 4 + \left[1 + 0.3 \exp\left(-\frac{(2\pi\rho-\pi)^2}{0.16}\right)\right] \cos(2\pi\rho)$, $y = \left[1 + 0.3 \exp\left(-\frac{(2\pi\rho-\pi)^2}{0.16}\right)\right] \sin(2\pi\rho)$, simulated with $k = 1$, $M = 100$, $T = 10$, $\Delta t = 0.01$.

To treat the nonlinearity in (2.3), we adopt a Picard-type iterative strategy at each time step. Given the iteration $(\mathbf{X}_i^{n+1,m}, V_i^{n+1,m}, \kappa_i^{n+1,m})$, the next iteration $(\mathbf{X}_i^{n+1,m+1}, V_i^{n+1,m+1}, \kappa_i^{n+1,m+1})$ is obtained by solving

$$\frac{\alpha_0 \mathbf{X}_i^{n+1,m+1} + \sum_{p=1}^k \alpha_p \mathbf{X}_i^{n+1-p}}{\Delta t} \cdot \mathbf{n}_i^{n+1,m} = V_i^{n+1,m+1}, \quad (2.4a)$$

$$V_i^{n+1,m+1} = \frac{\delta_{\rho\rho} \kappa_i^{n+1,m+1}}{|\delta_{\rho} \mathbf{X}_i^{n+1,m}|^2} - \frac{\delta_{\rho} \kappa_i^{n+1,m} \delta_{\rho} \mathbf{X}_i^{n+1,m} \cdot \delta_{\rho\rho} \mathbf{X}_i^{n+1,m+1}}{|\delta_{\rho} \mathbf{X}_i^{n+1,m}|^4} + \frac{1}{2} (\kappa_i^{n+1,m})^2 \kappa_i^{n+1,m+1}, \quad (2.4b)$$

$$\kappa_i^{n+1,m+1} \mathbf{n}_i^{n+1,m} = -\frac{\delta_{\rho\rho} \mathbf{X}_i^{n+1,m+1}}{|\delta_{\rho} \mathbf{X}_i^{n+1,m}|^2} + \frac{\tau_i^{n+1,m} \cdot \delta_{\rho\rho} \mathbf{X}_i^{n+1,m+1}}{|\delta_{\rho} \mathbf{X}_i^{n+1,m}|^3} \delta_{\rho} \mathbf{X}_i^{n+1,m+1}. \quad (2.4c)$$

The iteration is terminated once

$$\max_i (\|\mathbf{X}_i^{n+1,m+1} - \mathbf{X}_i^{n+1,m}\| + |V_i^{n+1,m+1} - V_i^{n+1,m}| + |\kappa_i^{n+1,m+1} - \kappa_i^{n+1,m}|) < \varepsilon_{\text{tol}},$$

where ε_{tol} is a prescribed tolerance. Upon convergence, we set

$$(\mathbf{X}_i^{n+1}, V_i^{n+1}, \kappa_i^{n+1}) = (\mathbf{X}_i^{n+1,m+1}, V_i^{n+1,m+1}, \kappa_i^{n+1,m+1}).$$

Remark 2. Numerical results shown in Figs. 2.1–2.2 indicate that the BDFk-FDM generally maintains high mesh quality and produces stable and reliable results for nearly convex or mildly perturbed curves with smooth geometric variation, as illustrated in Fig. 2.1. However, when the evolving curve contains more intricate geometric features or undergoes rapid curvature changes, as in the examples of Fig. 2.2, the mesh may gradually develop noticeable stretching, clustering, or other forms of nonuniformity during the evolution. For strongly oscillatory interfaces with sharp tips or drastic curvature transitions, the geometric quantities become highly sensitive from the very beginning, making the discrete system strongly nonlinear and stiff; in such cases, pronounced mesh tangling and even numerical breakdown may occur. These observations highlight the necessity of incorporating more effective mesh redistribution strategies in order to accurately capture the evolution of geometrically complex interfaces.

3. A-WAR algorithm

In this section, we introduce an adaptive mesh redistribution algorithm for the Willmore flow to improve the quality of the evolving mesh. The A-WAR algorithm is presented, which augments the WAR framework with an adaptive monitor function. Motivated by the sensitivity of mesh distribution to geometric complexity (see Remark 2), our goal is to adjust the nodal positions dynamically according to the local geometric features of the curve. The methods developed here provide systematic procedures for obtaining a more balanced and geometrically consistent discretization. The exposition is organized as follows: the first subsection introduces the WAR framework, and the second subsection presents the adaptive monitor-selection mechanism and the complete A-WAR algorithm.

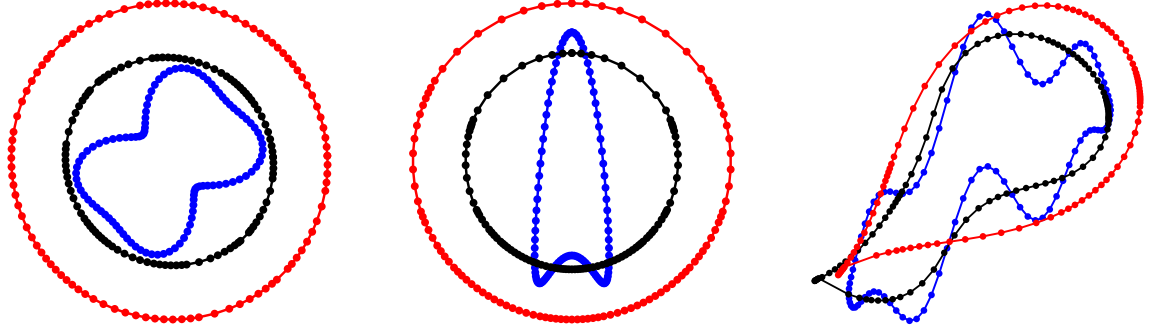


Figure 2.2: Representative examples showing mesh degradation under complex interface geometries. The blue, black, and red curves represent the initial curve, the evolved curve at the mid-time, and the final curve, respectively. Left: the initial curves are given by $x = \cos(2\pi\rho)[1 + 0.3 \sin(4\pi\rho) + 0.2 \cos(8\pi\rho)]$, $y = \sin(2\pi\rho)[1 + 0.3 \sin(4\pi\rho) + 0.2 \cos(8\pi\rho)]$, simulated with $k = 1$, $M = 100$, $T = 10$, $\Delta t = 0.01$. Middle: the initial curves are given by $x = 0.5 \sin(2\pi\rho)$, $y = 1.5 \cos(2\pi\rho)[1 + \cos(2\pi\rho)]$, simulated with $k = 1$, $M = 100$, $T = 10$, $\Delta t = 0.01$. Right: the initial curves are given by $x = 1.2 \cos(2\pi\rho)$, $y = 0.5 \sin(2\pi\rho) + \sin(\cos(2\pi\rho)) + \sin(2\pi\rho)[0.2 + \sin(2\pi\rho) \sin^2(6\pi\rho)]$, simulated with $k = 1$, $M = 100$, $T = 1$, $\Delta t = 0.0001$.

3.1. WAR framework

To enhance mesh quality during the evolution of a closed planar curve, we adopt a WAR strategy based on the principle of weighted equidistribution. Let the evolving interface be represented by the periodic parametrization $\mathbf{X}(\rho, t) = (x(\rho, t), y(\rho, t))^T$, $\rho \in [0, 1]$, and denote its classical arc-length element by $|\partial_\rho \mathbf{X}| d\rho$. A common approach to adaptive mesh refinement in geometric evolution problems is to introduce a monitor function $m(\rho, t)$, a strictly positive quantity that reflects the local geometric complexity of the curve. Interpreting m as a density, larger values of $m(\rho, t)$ indicate regions where finer mesh resolution is required, while smaller values correspond to flatter areas that need fewer points. Following this idea, we define the weighted arc-length element

$$m(\rho, t) |\partial_\rho \mathbf{X}| d\rho$$

and the cumulative weighted arc-length

$$w(\rho, t) = \int_0^\rho m(q, t) |\partial_q \mathbf{X}| dq, \quad L_w(t) = w(1, t).$$

From a numerical point of view, the WAR framework operates entirely on the discrete nodal points. Given the nodal parameters $\{\rho_j\}_{j=0}^M$, the coordinates $\{\mathbf{X}_j\}_{j=0}^M$, and the monitor values $\{m_j\}_{j=0}^M$ at time level t^{n+1} , we first compute the segment lengths

$$\Delta s_j = \|\mathbf{X}_{j+1} - \mathbf{X}_j\|, \quad j = 0, \dots, M-1,$$

and then the weighted segment lengths

$$\omega_j = \frac{1}{2}(m_j + m_{j+1})\Delta s_j.$$

The discrete cumulative weighted arc-length is defined by

$$w_0 = 0, \quad w_j = \sum_{k=0}^{j-1} \omega_k, \quad j = 1, \dots, M,$$

with total weighted length $L_w = w_M$. In the WAR framework, the goal is to redistribute the nodes so that each mesh interval carries the same amount of weighted arc-length. To enforce this in discrete form, we introduce the equidistributed target values

$$w_i^{\text{tar}} = \frac{i}{M} L_w, \quad i = 0, \dots, M,$$

which implies that

$$w_i^{\text{tar}} - w_{i-1}^{\text{tar}} = \frac{L_w}{M}, \quad i = 1, \dots, M.$$

The updated parameter locations $\{\rho_i^{\text{new}}\}_{i=0}^M$ are then obtained by inverting the discrete, strictly increasing mapping $w_j \mapsto \rho_j$. For each target value w_i^{tar} , we locate the unique interval

$$w_j \leq w_i^{\text{tar}} \leq w_{j+1},$$

and apply a linear interpolation within this interval:

$$\rho_i^{\text{new}} = \rho_j + \frac{w_i^{\text{tar}} - w_j}{w_{j+1} - w_j} (\rho_{j+1} - \rho_j).$$

Repeating this for $i = 0, \dots, M$ yields the full set of redistributed parameter values. Finally, the new nodal positions are obtained by evaluating the curve at these updated parameters,

$$\mathbf{X}_i^{\text{new}} = \mathbf{X}(\rho_i^{\text{new}}).$$

The complete numerical procedure is summarized in Algorithm 1.

Algorithm 1 WAR framework (subroutine for A-WAR algorithm).

Input: The values of $\mathbf{X}_j := \mathbf{X}_j^{n+1}$, computed by the BDFk-FDMs. and monitor values m_j , $j = 1, \dots, M$.

- **Step 1: Compute segment lengths.** Compute the discrete arc-length increments $\Delta s_j = \|\mathbf{X}_{j+1} - \mathbf{X}_j\|$, $j = 0, \dots, M - 1$.
- **Step 2: Compute weighted lengths.** Compute the weighted lengths using the monitor function:

$$\omega_j = \frac{1}{2}(m_j + m_{j+1}) \Delta s_j.$$

- **Step 3: Compute cumulative weighted arc-length.** Form the cumulative sum

$$w_0 = 0, \quad w_j = \sum_{k=0}^{j-1} \omega_k, \quad j = 1, \dots, M,$$

and set the total weighted length $L_w = w_M$.

- **Step 4: Define target distribution.** Construct the equidistributed target points

$$w_i^{\text{tar}} = \frac{i}{M} L_w, \quad i = 0, \dots, M.$$

- **Step 5: Redistribute the nodes.** Determine the new parameters ρ_i^{new} by interpolating the discrete mapping $w_j \mapsto \rho_j$ at the target values w_i^{tar} , and evaluate the curve at ρ_i^{new} to obtain $\mathbf{X}_i^{\text{new}}$.

- **Step 6: Enforce periodicity.** Set $\mathbf{X}_0^{\text{new}} = \mathbf{X}_M^{\text{new}}$, and replace the old interface by $\mathbf{X}_j \leftarrow \mathbf{X}_j^{\text{new}}$, which will be used as the input for the next time step of the BDFk-FDMs.

Remark 3. In the WAR framework shown in Algorithm 1, the monitor function m_j plays a central role in determining the quality of the mesh redistribution. However, manually prescribing the monitor function at each time step based on the initial geometry or heuristic considerations is both difficult to perform and often insufficiently accurate. A fixed or preassigned monitor function typically fails to capture the local geometric variations that arise during the evolution of the curve, such as the rapid refinement required in high-curvature regions, the excessive sparsity in flatter regions, or the overall nonuniform stretching of the mesh. In view of these limitations, it is essential to construct the monitor function in an adaptive manner so that it can respond to the current geometric complexity of the evolving curve. To this end, in the next subsection we introduce Algorithm 2, which provides an adaptive procedure for selecting the monitor function and determining its parameters based on curvature- and mesh-related indicators. The resulting monitor values $\{m_j\}$ accurately reflect the instantaneous geometric features of the curve and serve as the input to Algorithm 1.

3.2. A-WAR algorithm

Having established the WAR framework in the previous subsection, we now turn to the construction of the monitor function, which determines how the mesh resolution should be distributed along the evolving curve. The goal is to design a mechanism that reacts to the local geometric characteristics of the curve, so that regions requiring higher resolution receive a proportionally larger weight. To achieve this, we introduce an adaptive selection strategy that evaluates several geometric indicators, including curvature-based quantities and mesh-quality measures, and determines the appropriate monitor model along with its parameters. Once the monitor values are computed, they are incorporated into the redistribution procedure to obtain the updated meshes.

Given a discrete curve represented by the points $\mathbf{X}_i = (x_i, y_i)$, $i = 1, \dots, M$, together with the corresponding curvature values κ_i , we begin by reconstructing the arc-length parameter s_i . This is done by computing the local segment lengths $\Delta s_i = \|\mathbf{X}_{i+1} - \mathbf{X}_i\|$, and defining s_i as their cumulative sum. The arc-length parametrization provides a natural coordinate along the curve and enables the evaluation of derivatives with respect to arc-length. To approximate the arc-length derivative of curvature, we employ the centered finite-difference operator

$$\delta_s \kappa_i := \frac{\kappa_{i+1} - \kappa_{i-1}}{s_{i+1} - s_{i-1}} = \frac{\kappa_{i+1} - \kappa_{i-1}}{\Delta s_i + \Delta s_{i-1}},$$

so that

$$\partial_s \kappa_i \approx \delta_s \kappa_i.$$

This discrete quantity measures the rate at which curvature varies along the curve. From these geometric quantities, we then define the following three key indicators:

$$C_0 = \max_i |\kappa_i|, \quad C_1 = \max_i |\delta_s \kappa_i|, \quad Q = \frac{\max_i \Delta s_i}{\min_i \Delta s_i}.$$

The first indicator, C_0 , represents the maximum curvature magnitude and characterizes the strongest bending present in the geometry. The second indicator, C_1 , reflects the maximal rate of curvature variation and thus captures the geometric complexity of the curve: rapid curvature oscillations or sharp transitions lead to large values of C_1 . The third indicator, Q , assesses the mesh quality by measuring the ratio between the largest and smallest segment lengths; a value close to 1 indicates an almost uniform discretization, whereas a large value signals significant mesh distortion. Together, the indicators C_0 , C_1 , and Q provide a compact but informative description of both the geometric features of the curve and the quality of its discretization. They form the basis for adaptive decisions such as selecting an appropriate monitor function or determining when mesh redistribution is required during the evolution.

Denote

$$M_f = M_f(\kappa(\rho, t), \kappa_s(\rho, t)) := m(\rho, t).$$

The adaptive selection procedure consists of two stages. In the first stage, we identify the base curvature–response regime by comparing the indicator C_0 with two prescribed thresholds C_0^{low} and C_0^{high} . M_f^{base} denotes the baseline part of the monitor function, chosen according to the overall curvature level of the curve; it provides the fundamental curvature–response behavior on which the adaptive strategy builds:

- **Low-curvature regime.** If $C_0 < C_0^{\text{low}}$, the curve is globally smooth, and the linear curvature–response model is selected:

$$M_f^{\text{base}} = 1 + \alpha |\kappa|.$$

- **Moderate-curvature regime.** If $C_0^{\text{low}} \leq C_0 < C_0^{\text{high}}$, the curve exhibits moderate bending. In this regime, a hybrid model combining linear and quadratic responses is used:

$$M_f^{\text{base}} = 1 + \alpha \left[(1 - \beta) |\kappa| + \beta \kappa^2 \right], \quad 0 < \beta < 1.$$

- **High-curvature regime.** If $C_0 \geq C_0^{\text{high}}$, pronounced curvature is detected, and the quadratic response model is adopted:

$$M_f^{\text{base}} = 1 + \alpha \kappa^2.$$

Remark 4. The parameter β controls the relative contribution of the quadratic term in the hybrid model. Although the selection of β is not mandatory and any value in $(0, 1)$ may be adopted, numerical experiments indicate that $\beta = 0.3$ provides a favorable balance. Specifically, this choice introduces sufficient nonlinear sensitivity to capture moderate curvature while avoiding excessive mesh concentration that can arise when the quadratic term is overly weighted. Moreover, $\beta = 0.3$ enables a smooth transition between the purely linear model in low-curvature regimes and the purely quadratic model in high-curvature regimes, thereby ensuring stable and consistent performance across a wide range of geometric conditions.

Next, we determine whether the base model should be enhanced by incorporating the curvature derivative. This decision is made by comparing C_1 with two thresholds C_1^{low} and C_1^{high} :

- **Slow curvature-variation regime.** If $C_1 < C_1^{\text{low}}$, the curvature varies gradually along the curve, and no additional refinement is required; the monitor function is taken to be the previously selected base model.
- **Moderate curvature-variation regime.** If $C_1^{\text{low}} \leq C_1 < C_1^{\text{high}}$, local changes in curvature are noticeable, and a linear curvature-gradient contribution is introduced:

$$M_f = 1 + \alpha |\kappa| + \gamma |\kappa_s|.$$

This enhancement allocates additional resolution to regions where curvature transitions occur.

- **Rapid curvature-variation regime.** If $C_1 \geq C_1^{\text{high}}$, the curvature exhibits sharp or highly oscillatory local variations. To capture such behavior, we employ the high-order combined model

$$M_f = 1 + \alpha \sqrt{\kappa^2 + \gamma \kappa_s^2},$$

which increases sensitivity to both curvature magnitude and curvature gradients in a balanced manner.

Algorithm 2 A-WAR algorithm: adaptive monitor selection and weighted mesh redistribution.

Input. The values of $\mathbf{X}_j := \mathbf{X}_j^{n+1}$, $j = 1, \dots, M$, computed by the BDFk-FDMs.

- **Step 1: Compute geometric indicators.** Reconstruct arc-length s_j and segment lengths

$$\Delta s_j = \|\mathbf{X}_{j+1} - \mathbf{X}_j\|.$$

Compute the discrete curvature derivative

$$\delta_s \kappa_j := \frac{\kappa_{j+1} - \kappa_{j-1}}{s_{j+1} - s_{j-1}} = \frac{\kappa_{j+1} - \kappa_{j-1}}{\Delta s_j + \Delta s_{j-1}},$$

and evaluate

$$C_0 = \max_j |\kappa_j|, \quad C_1 = \max_j |\delta_s \kappa_j|, \quad Q = \frac{\max_j \Delta s_j}{\min_j \Delta s_j}.$$

- **Step 2: Select base curvature-response model (using C_0).** Using thresholds C_0^{low} and C_0^{high} :

- If $C_0 < C_0^{\text{low}}$: select **Low-curvature regime**.
- If $C_0^{\text{low}} \leq C_0 < C_0^{\text{high}}$: select **Moderate-curvature regime**.
- If $C_0 \geq C_0^{\text{high}}$: select **High-curvature regime**.

- **Step 3: Apply curvature-variation enhancement (using C_1).** Using thresholds C_1^{low} and C_1^{high} :

- If $C_1 < C_1^{\text{low}}$: no enhancement; retain the base model.
- If $C_1^{\text{low}} \leq C_1 < C_1^{\text{high}}$: enhance with **Moderate curvature-variation variation regime**.
- If $C_1 \geq C_1^{\text{high}}$: enhance with **Rapid curvature-variation regime**.

- **Step 4: Set monitor parameters.** Initialize

$$\alpha = \alpha_0, \quad \gamma = \gamma_0,$$

and store (α, γ) together with the selected model type.

- **Step 5: Evaluate the monitor.** For each node, compute

$$m_j = \text{monitor.eval}(\kappa_j, \delta_s \kappa_j).$$

- **Step 6: Perform weighted arc-length redistribution.** Use the monitor values $\{m_j\}$, together with the current nodal parameters $\{\rho_j\}$ and coordinates $\{\mathbf{X}_j\}$, as input to Algorithm 1 (WAR framework) to obtain the updated nodal coordinates $\{\mathbf{X}_j^{\text{new}}\}_{j=0}^M$.

Output. Updated nodal coordinates $\{\mathbf{X}_j^{\text{new}}\}_{j=0}^M$ after A-WAR redistribution.

The parameters α and γ are initialized by user-specified values α_0 and γ_0 , respectively, and may be further adjusted based on mesh quality during subsequent steps of the algorithm. Moreover, once the curvature-gradient indicator exceeds the lower threshold C_1^{low} , the gradient contribution becomes significant, and the corresponding enhanced monitor (either the linear form including $|\kappa_j|$ or the high-order combined form) replaces the baseline model selected in the first stage. The complete procedure for selecting the monitor function from the geometric indicators C_0 , C_1 , and Q is summarized in Algorithm 2.

Remark 5. The quantity Q measures the nonuniformity of the current mesh. A value $Q \approx 1$ indicates that the mesh is nearly uniform, whereas a large Q indicates significant mesh distortion, with some segments being overly dense and others excessively sparse. In the A-WAR algorithm, Q is employed to adaptively adjust the monitor parameters α and γ : when Q exceeds prescribed thresholds, these parameters are amplified to increase the sensitivity of the monitor to curvature and curvature gradients. This enhancement enables the subsequent weighted arc-length redistribution to more effectively improve mesh quality and prevent further mesh degradation.

Algorithms 1 and 2 together define the proposed A-WAR algorithm. Algorithm 1 provides the WAR framework, which prescribes how the mesh nodes are repositioned once a set of monitor values is given. Algorithm 2 supplies these monitor values through an adaptive procedure based on geometric indicators of the evolving interface. The complete A-WAR algorithm is therefore obtained by first constructing the monitor function via Algorithm 2 and then invoking the redistribution framework of Algorithm 1. In this way, the mesh is redistributed in a manner that automatically responds to the local geometric complexity of the curve.

Remark 6. In the existing literature, many numerical approaches, particularly PFEM-based methods, have been successfully applied to geometric evolution equations such as mean curvature flow, surface diffusion flow, and Willmore flow. A common criterion for evaluating these methods is whether the mesh remains uniformly distributed or asymptotically approaches such a configuration during the evolution. For the planar Willmore flow, the methods in [22, 26]

generate asymptotically uniform meshes, yet they do not explicitly account for geometric quantities such as curvature. Consequently, temporary mesh distortion may occur in regions with rapid geometric variation before uniformity is restored. We supply the A-WAR algorithm in Algorithm 2, where a curvature-based monitor function, incorporating both curvature magnitude and curvature variation, guides the redistribution of mesh nodes. This strategy concentrates points in highly curved regions as well as in regions with rapid curvature variation, while relaxing them elsewhere, yielding a mesh that adapts more closely to the evolving geometry. Such redistribution improves numerical robustness and maintains mesh consistency for high-order geometric flows, not only for the Willmore flow considered in this work, but also for a broad class of curvature-driven interface evolution problems.

To illustrate the qualitative behavior of the complete A-WAR algorithm, we now present three simple test curves. These examples demonstrate how the adaptive redistribution procedure affects the evolution of curves with different geometric features. The initial and evolved interfaces are shown in Fig 3.1. A comparison with the non-adaptive BDFk-FDM results in Fig. 2.2 further demonstrates the effectiveness of the proposed adaptive strategy. For the oscillatory interfaces in the left and middle panels of Fig. 3.1, the standard BDFk-FDM does not immediately break down, but the mesh rapidly becomes highly nonuniform and severely distorted as the curves evolve. For the more challenging, strongly oscillatory interface in the right panel of Fig. 3.1, the non-adaptive method performs even worse: pronounced mesh tangling appears at an early stage, eventually leading to a numerical singularity and premature termination of the computation. Fig. 3.1 demonstrates that the A-WAR algorithm successfully maintains a well-distributed mesh and produces stable, smooth interface dynamics, in clear contrast to the inferior performance of the non-adaptive scheme. These observations highlight that adaptive monitor-driven redistribution is crucial for preventing mesh degeneration and ensuring robust simulations of curvature-driven flows.

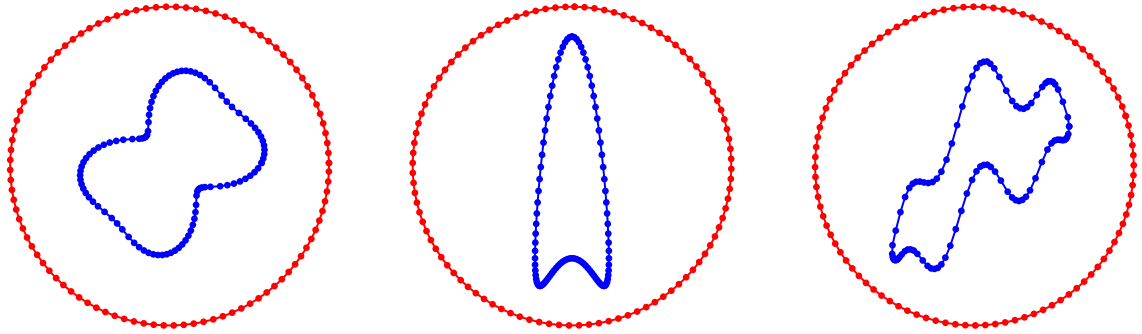


Figure 3.1: Evolution of several closed curves with pronounced oscillations and high-curvature features used to test the Algorithm 2. Blue curves represent the initial curves, and red curves represent the evolved curves at the final time. Left: the initial curves are given by $x = [1 + 0.3 \sin(4\pi\rho) + 0.2 \cos(8\pi\rho)] \cdot \cos(2\pi\rho)$, $y = [1 + 0.3 \sin(4\pi\rho) + 0.2 \cos(8\pi\rho)] \cdot \sin(2\pi\rho)$, simulated with $k = 1$, $M = 100$, $T = 10$, $\Delta t = 0.01$. Middle: the initial curves are given by $x = 0.5 \sin(2\pi\rho)$, $y = 1.5 \cos(2\pi\rho) [1 + \cos(2\pi\rho)]$, simulated with $k = 1$, $M = 100$, $T = 10$, $\Delta t = 0.01$. Right: the initial curves are given by $x = 1.2 \cos(2\pi\rho)$, $y = 0.5 \sin(2\pi\rho) + \sin(\cos(2\pi\rho)) + \sin(2\pi\rho) [0.2 + \sin(2\pi\rho) \sin^2(6\pi\rho)]$, simulated with $k = 1$, $M = 100$, $T = 10$, $\Delta t = 0.0001$.

4. A-BDFk-FDMs and EC algorithm

In addition to explicit mesh-redistribution techniques such as the A-WAR method introduced earlier, mesh adaptivity can also be achieved intrinsically through the evolution equation. A widely used approach is to introduce a suitable tangential velocity that does not affect the geometric motion of the interface but enables the parametrization to adjust continuously during the evolution. By incorporating such a tangential component, the mesh can redistribute itself in response to the local geometric features of the curve without requiring a separate post-processing step. In this section, we incorporate the tangential component directly into the evolution equation and examine its role in producing an adaptive parametrization for the evolving curve.

4.1. The new coupled system

The purpose of introducing a tangential component into the evolution of the curve is to regulate the parametrization without altering the geometric shape of the interface. Building on the equidistribution principle developed in the previous section, we now derive an explicit formula for the tangential velocity component that drives the mesh toward the desired adaptive distribution. The starting point is the observation that the parametrization is allowed to change along the tangent direction while the normal component remains dictated solely by the geometric evolution law.

We aim to redistribute mesh points along the evolving curve $\mathbf{X}(\rho, t)$ according to a prescribed monitor function $M_f(\kappa, \kappa_s, t) > 0$. Let $s(\rho, t)$ denote the arc-length coordinate, as defined in Section 2.1. From the definition of s , we have

the relationship

$$\partial_\rho s = |\partial_\rho \mathbf{X}|.$$

The equidistribution principle requires the weighted arc-length element $M_f ds$ to be uniformly distributed in ρ . In other words, there exists a time-dependent constant $C(t)$ such that

$$M_f(\kappa, \kappa_s, t) \partial_\rho s(\rho, t) = C(t).$$

By integrating this equation over the reference interval $[0, 1]$, we obtain

$$C(t) = \int_0^1 M_f(\kappa, \kappa_s, t) \partial_\rho s \, d\rho = \int_{\Gamma(t)} M_f(\kappa, \kappa_s, t) \, ds.$$

Differentiating this equation with respect to ρ gives the differential form of the equidistribution condition:

$$\partial_\rho (M_f(\kappa, \kappa_s, t) \partial_\rho s) = 0.$$

To derive the tangential velocity that enforces this condition, we introduce the inverse parametrization $\rho = \rho(s, t)$ and define the functional

$$\mathcal{I}[\rho] = \frac{1}{2} \int_{\Gamma(t)} \frac{1}{M_f} (\partial_s \rho)^2 \, ds.$$

This choice of functional is motivated by the observation that if $\partial_s \rho$ is proportional to M_f , the computational parameter will allocate more arc-length to regions where M_f is larger, thus increasing the mesh density in these regions, which is precisely the desired effect of equidistribution.

Lemma 4.1. *The evolution of the arc-length coordinate s required to enforce the equidistribution condition is given by*

$$\partial_t s = -\frac{1}{\partial_s \rho} \frac{P}{\mathcal{J}} \partial_s \left(\frac{1}{M_f} \partial_s \rho \right),$$

where $\mathcal{J} > 0$ is a relaxation time constant, and P is a positive operator that controls the smoothing properties of the redistribution process.

Proof. To compute the variational derivative of the functional $\mathcal{I}[\rho]$, we perturb ρ by $\rho + \varepsilon \eta$, where η is an arbitrary variation that vanishes at the boundaries. Applying integration by parts, we obtain

$$\frac{d}{d\varepsilon} \mathcal{I}[\rho + \varepsilon \eta] \Big|_{\varepsilon=0} = \int_{\Gamma(t)} \frac{1}{M_f} (\partial_s \rho) (\partial_s \eta) \, ds = - \int_{\Gamma(t)} \partial_s \left(\frac{1}{M_f} \partial_s \rho \right) \eta \, ds.$$

Since this identity holds for all admissible variations η , we conclude that the variational derivative is:

$$\frac{\delta \mathcal{I}}{\delta \rho} = -\partial_s \left(\frac{1}{M_f} \partial_s \rho \right).$$

For stationary points of the functional \mathcal{I} , the Euler-Lagrange equation must hold

$$\partial_s \left(\frac{1}{M_f} \partial_s \rho \right) = 0,$$

which corresponds to the differential equidistribution condition.

To drive the parametrization toward the equilibrium condition, we introduce a relaxation dynamics for the inverse mapping $\rho(s, t)$. Specifically, by evolving ρ in the direction of the negative gradient of the functional \mathcal{I} , we obtain

$$\partial_t \rho = -\frac{P}{\mathcal{J}} \frac{\delta \mathcal{I}}{\delta \rho} = \frac{P}{\mathcal{J}} \partial_s \left(\frac{1}{M_f} \partial_s \rho \right), \quad (4.1)$$

where $\mathcal{J} > 0$ is a relaxation time constant, and P is a positive operator that controls the smoothing properties of the redistribution process. This evolution ensures that the functional \mathcal{I} decreases monotonically over time, and the parametrization asymptotically approaches the equidistribution condition. Then, by using the identity $\rho = \rho(s(\rho, t), t)$, which is valid for all (ρ, t) , and differentiating with respect to s while keeping t fixed, we obtain

$$\partial_\rho s = \frac{1}{\partial_s \rho}. \quad (4.2)$$

Differentiating (4.2) with respect to t , we derive

$$\partial_t s = -\frac{\partial_t \rho}{\partial_s \rho}. \quad (4.3)$$

Substituting (4.1) into (4.3) gives

$$\partial_t s = -\frac{1}{\partial_s \rho} \frac{P}{\mathcal{J}} \partial_s \left(\frac{1}{M_f} \partial_s \rho \right).$$

Therefore, the evolution equation for the arc-length coordinate s is derived. \square

Using Lemma 4.1, we derive the equation for the total velocity.

Lemma 4.2. *The total velocity of the curve evolution is given by*

$$\partial_t \mathbf{X} = V \mathbf{n} + \left[\frac{P}{\mathcal{J}} (M_f |\partial_\rho \mathbf{X}|)^{-2} \partial_\rho (M_f |\partial_\rho \mathbf{X}|) \right] \boldsymbol{\tau}. \quad (4.4)$$

Proof. Let $Q := M_f \partial_\rho s$. Then, we have

$$\partial_s \left(\frac{1}{M_f} \partial_s \rho \right) = \partial_s \left(\frac{1}{Q} \right) = -\frac{\partial_s Q}{Q^2}. \quad (4.5)$$

From Lemma 4.1, we obtain

$$\partial_t s = \frac{1}{\partial_s \rho} \frac{P}{\mathcal{J}} \frac{\partial_s Q}{Q^2} = \frac{1}{\partial_s \rho} \frac{P}{\mathcal{J}} \frac{\partial_s Q}{(M_f \partial_\rho s)^2} = \frac{P}{\mathcal{J}} \frac{\partial_s Q}{M_f Q}. \quad (4.6)$$

Hence, by using

$$\partial_s Q = \frac{M_f}{Q} \partial_\rho Q,$$

in (4.6), we have

$$\partial_t s = \frac{P}{\mathcal{J}} \frac{M_f}{Q} \cdot \frac{\partial_\rho Q}{M_f Q} = \frac{P}{\mathcal{J}} \frac{\partial_\rho Q}{Q^2} = \frac{P}{\mathcal{J}} (M_f \partial_\rho s)^{-2} \partial_\rho (M_f \partial_\rho s). \quad (4.7)$$

The curve evolution at fixed ρ is given by

$$\partial_t \mathbf{X} \Big|_\rho = \partial_t \mathbf{X} \Big|_s + \boldsymbol{\tau} \partial_t s.$$

Since $\partial_t \mathbf{X} \Big|_s$ contributes only to the normal motion, we obtain the tangential velocity:

$$\partial_t \mathbf{X} \cdot \boldsymbol{\tau} = \partial_t s. \quad (4.8)$$

By virtue of (4.7) and (4.8), we get

$$\partial_t \mathbf{X} \cdot \boldsymbol{\tau} = \frac{P}{\mathcal{J}} (M_f \partial_\rho s)^{-2} \partial_\rho (M_f \partial_\rho s) = \frac{P}{\mathcal{J}} (M_f |\partial_\rho \mathbf{X}|)^{-2} \partial_\rho (M_f |\partial_\rho \mathbf{X}|).$$

Finally, since the normal component of the curve evolution is given by $\partial_t \mathbf{X} \cdot \mathbf{n} = V$ from (2.2a), we conclude

$$\partial_t \mathbf{X} = (\partial_t \mathbf{X} \cdot \mathbf{n}) \mathbf{n} + (\partial_t \mathbf{X} \cdot \boldsymbol{\tau}) \boldsymbol{\tau} = V \mathbf{n} + \left[\frac{P}{\mathcal{J}} (M_f |\partial_\rho \mathbf{X}|)^{-2} \partial_\rho (M_f |\partial_\rho \mathbf{X}|) \right] \boldsymbol{\tau}.$$

Therefore, we have completed the proof. \square

We couple the total velocity (4.4) with the original Willmore flow (2.2) to obtain the following adaptive moving mesh formulation. Given the initial curve $\mathbf{X}(\rho, 0) = \mathbf{X}^0(\rho)$, we seek $(\mathbf{X}(\rho, t), V(\rho, t), \kappa(\rho, t))$, $(\rho, t) \in \mathbb{T} \times (0, +\infty)$, such that

$$\partial_t \mathbf{X} = V \mathbf{n} + \left[\frac{P}{\mathcal{J}} (M_f |\partial_\rho \mathbf{X}|)^{-2} \partial_\rho (M_f |\partial_\rho \mathbf{X}|) \right] \boldsymbol{\tau}, \quad (4.9a)$$

$$V = \frac{\partial_{\rho\rho} \kappa}{|\partial_\rho \mathbf{X}|^2} - \frac{\partial_\rho \kappa \partial_\rho \mathbf{X} \cdot \partial_{\rho\rho} \mathbf{X}}{|\partial_\rho \mathbf{X}|^4} + \frac{1}{2} \kappa^3, \quad (4.9b)$$

$$\kappa = -\frac{\partial_{\rho\rho} \mathbf{X} \cdot \mathbf{n}}{|\partial_\rho \mathbf{X}|^2}. \quad (4.9c)$$

Remark 7. Since the adaptive moving mesh Willmore system (4.9) introduces an additional tangential velocity (4.4), the third equation in (4.9), which defines the curvature κ , needs to be reformulated accordingly. This modification ensures consistency between the geometric definition of curvature and the new tangential motion, allowing the system to maintain correct geometric evolution under the adaptive mesh redistribution.

Remark 8. The tangential velocity equation has been extensively studied in the literature [33, 37] and has recently been applied to the forced mean curvature flow [36]. In the present work, we extend this framework to the Willmore flow by employing a full velocity formulation. In comparison with the forced mean curvature flow, the Willmore flow exhibits significantly more complex geometric structures and involves higher-order curvature terms, rendering its evolution substantially more intricate and challenging from both analytical and numerical perspectives. Furthermore, in order to more thoroughly investigate these additional complexities, we consider more sophisticated forms of the monitor function. In particular, beyond the curvature κ itself, we also incorporate derivatives of curvature κ_s and the squared curvature κ^2 , into the monitor function to better capture localized geometric variations along the interface. In addition, we compare our results with those obtained using BDFk-FDMs that do not incorporate the tangential velocity component. Through this comparison, we highlight the advantages of introducing a tangential velocity component, demonstrating its superior ability to preserve mesh quality, accurately capture flow evolution, and achieve higher numerical accuracy.

4.2. Finite difference discretizations

Prior to the spatial discretization, we slightly reformulate the curve evolution equation (4.9a) to obtain a form that is more convenient for numerical implementation. Recalling that

$$\partial_\rho |\partial_\rho \mathbf{X}| = \frac{\partial_\rho \mathbf{X} \cdot \partial_{\rho\rho} \mathbf{X}}{|\partial_\rho \mathbf{X}|},$$

we can expand (4.9a) and express it as

$$\partial_t \mathbf{X} = V \mathbf{n} + \left[\frac{P}{\mathcal{J}} \frac{\partial_\rho M_f \partial_\rho \mathbf{X} + M_f \partial_{\rho\rho} \mathbf{X}}{(M_f |\partial_\rho \mathbf{X}|)^2} \cdot \boldsymbol{\tau} \right] \boldsymbol{\tau}. \quad (4.10)$$

Using the definition of $\boldsymbol{\tau}$ given in (2.1), the above relation can be reorganized into the equivalent form

$$\partial_t \mathbf{X} = V \mathbf{n} + \left[\left(\frac{P M_f}{(\mathcal{J} (M_f |\partial_\rho \mathbf{X}|)^2)} \partial_{\rho\rho} \mathbf{X} \right) \cdot \boldsymbol{\tau} + \frac{P \partial_\rho M_f |\partial_\rho \mathbf{X}|}{\mathcal{J} (M_f |\partial_\rho \mathbf{X}|)^2} \right] \boldsymbol{\tau}. \quad (4.11)$$

We next present the discrete formulations of the adaptive moving mesh Willmore system (4.9). Following the same discretization strategy as in Section 2.2, we employ second-order centered finite differences for spatial derivatives and the BDFk for temporal discretization. Let $\{(\mathbf{X}_i^{n-p}, V_i^{n-p}, \kappa_i^{n-p})\}_{p=0}^{k-1}$ be the known solution values at previous time levels. Then, we employ the following A-BDFk-FDMs to numerically solve the adaptive moving mesh Willmore system (4.9):

$$\frac{1}{\Delta t} \sum_{p=0}^k \alpha_p \mathbf{X}_i^{n+1-p} = V_i^{n+1} \mathbf{n}_i^{n+1} + \left[\left(\frac{P_i^{n+1} M_{f,i}^{n+1}}{(\mathcal{J} (M_{f,i}^{n+1} |\partial_\rho \mathbf{X}_i^{n+1}|)^2)} \delta_{\rho\rho} \mathbf{X}_i^{n+1} \right) \cdot \boldsymbol{\tau}_i^{n+1} + \frac{P_i^{n+1} \delta_\rho M_{f,i}^{n+1} |\partial_\rho \mathbf{X}_i^{n+1}|}{\mathcal{J} (M_{f,i}^{n+1} |\partial_\rho \mathbf{X}_i^{n+1}|)^2} \right] \boldsymbol{\tau}_i^{n+1}, \quad (4.12a)$$

$$V_i^{n+1} = \frac{\delta_{\rho\rho} \kappa_i^{n+1}}{|\partial_\rho \mathbf{X}_i^{n+1}|^2} - \frac{\delta_\rho \kappa_i^{n+1} (\delta_\rho \mathbf{X}_i^{n+1} \cdot \delta_{\rho\rho} \mathbf{X}_i^{n+1})}{|\partial_\rho \mathbf{X}_i^{n+1}|^4} + \frac{1}{2} (\kappa_i^{n+1})^3, \quad (4.12b)$$

$$\kappa_i^{n+1} = -\frac{\delta_{\rho\rho} \mathbf{X}_i^{n+1} \cdot \mathbf{n}_i^{n+1}}{|\partial_\rho \mathbf{X}_i^{n+1}|^2}. \quad (4.12c)$$

Here, δ_ρ and $\delta_{\rho\rho}$ denote the second-order centered finite-difference operators for the first and second spatial derivatives, respectively, and the coefficients α_p are the BDFk weights that have been defined in Section 2.2.

To efficiently solve the A-BDFk-FDMs, we employ a Picard-type iterative procedure at every time step. This approach updates the geometric variables through a sequence of linearized problems until convergence is achieved. Starting from the iteration $(\mathbf{X}_i^{n+1,m}, V_i^{n+1,m}, \kappa_i^{n+1,m})$, the subsequent iteration $(\mathbf{X}_i^{n+1,m+1}, V_i^{n+1,m+1}, \kappa_i^{n+1,m+1})$ is determined by solving

$$\frac{\alpha_0 \mathbf{X}_i^{n+1,m+1} + \sum_{p=1}^k \alpha_p \mathbf{X}_i^{n+1-p}}{\Delta t} = \left[\left(\frac{P_i^{n+1,m} M_{f,i}^{n+1,m}}{(\mathcal{J} (M_{f,i}^{n+1,m} |\partial_\rho \mathbf{X}_i^{n+1,m}|)^2)} \delta_{\rho\rho} \mathbf{X}_i^{n+1,m+1} \right) \cdot \boldsymbol{\tau}_i^{n+1,m} \right] \boldsymbol{\tau}_i^{n+1,m}$$

$$+ \left(\frac{P_i^{n+1,m} \delta_\rho M_{f,i}^{n+1,m} |\delta_\rho \mathbf{X}_i^{n+1,m}|}{\mathcal{J}(M_{f,i}^{n+1,m} |\delta_\rho \mathbf{X}_i^{n+1,m}|)^2} \right) \boldsymbol{\tau}_i^{n+1,m} + V_i^{n+1,m+1} \mathbf{n}_i^{n+1,m}, \quad (4.13a)$$

$$V_i^{n+1,m+1} = \frac{\delta_{\rho\rho} \kappa_i^{n+1,m+1}}{|\delta_\rho \mathbf{X}_i^{n+1,m}|^2} - \frac{\delta_\rho \kappa_i^{n+1,m} (\delta_\rho \mathbf{X}_i^{n+1,m} \cdot \delta_{\rho\rho} \mathbf{X}_i^{n+1,m+1})}{|\delta_\rho \mathbf{X}_i^{n+1,m}|^4} + \frac{1}{2} (\kappa_i^{n+1,m})^2 \kappa_i^{n+1,m+1}, \quad (4.13b)$$

$$\kappa_i^{n+1,m+1} = - \frac{\delta_{\rho\rho} \mathbf{X}_i^{n+1,m+1} \cdot \mathbf{n}_i^{n+1,m}}{|\delta_\rho \mathbf{X}_i^{n+1,m}|^2}. \quad (4.13c)$$

The iteration continues until the following stopping criterion is satisfied:

$$\max_i (\|\mathbf{X}_i^{n+1,m+1} - \mathbf{X}_i^{n+1,m}\| + |V_i^{n+1,m+1} - V_i^{n+1,m}| + |\kappa_i^{n+1,m+1} - \kappa_i^{n+1,m}|) < \varepsilon_{\text{tol}}.$$

Once this tolerance criterion is satisfied, we set

$$(\mathbf{X}_i^{n+1}, V_i^{n+1}, \kappa_i^{n+1}) = (\mathbf{X}_i^{n+1,m+1}, V_i^{n+1,m+1}, \kappa_i^{n+1,m+1}).$$

Remark 9. During the numerical simulations with the A-BDFk-FDMs, two strategies are considered for the choice of the monitor function. Specifically, the monitor function may be prescribed as a fixed function prior to the computation, or it may be updated adaptively according to the behavior of the discrete solution, following the A-WAR algorithm. The latter strategy allows the mesh distribution to respond dynamically to the evolving features of the solution.

4.3. EC algorithm

Although the A-BDFk-FDMs (4.12) exhibit energy stability in numerical experiments, establishing such stability at the theoretical level remains challenging. This difficulty motivates us to develop the following EC algorithm, which guarantees the stability of the approximate energy. To this end, we begin at the continuous level. Let $W(t)$ denote the continuous Willmore energy of the evolving curve, given by (1.1). We introduce the new continuous energy

$$W_c(t) = W(t) + C, \quad C > 0,$$

where the constant C ensures that $W_c(t)$ remains strictly positive. Since C is independent of time, the modified energy satisfies [26, 38]

$$\frac{dW_c(t)}{dt} = \frac{dW(t)}{dt} = - \int_0^1 V^2 |\partial_\rho \mathbf{X}| d\rho. \quad (4.14)$$

We further introduce an auxiliary scalar variable $R(t)$ associated with $W_c(t)$, defined by

$$R(t) = W_c(t),$$

which will be used in the construction of the discrete algorithm.

At the discrete time level $t = t^n$, the numerical solution is written as $\mathbf{U}^n = (\mathbf{X}_i^n, V_i^n, \kappa_i^n)$, and the discrete Willmore energy is defined by

$$W^n = W(\mathbf{U}^n) = \frac{1}{2} \sum_{i=1}^M (\kappa_i^n)^2 |\delta_\rho \mathbf{X}_i^n|.$$

Correspondingly, we introduce the new discrete energy

$$W_c^n = W^n + C,$$

together with a discrete auxiliary variable R^n designed to satisfy the monotonicity condition

$$R^{n+1} \leq R^n.$$

Once R^{n+1} is updated, a global scaling is applied to enforce consistency between R^{n+1} and the geometric energy W^{n+1} . Based on these considerations, we now present an EC algorithm in Algorithm 3.

Theorem 4.1 (Energy stability). *For the A-BDFk-FDMs together with the EC algorithm, the discrete energy is unconditionally stable in the sense that*

$$R^{n+1} - R^n = -\Delta t \frac{R^{n+1}}{W_c^{n+1}} D^{n+1} \leq 0,$$

where $D^{n+1} > 0$ is defined in Algorithm 3.

Algorithm 3 EC algorithm.

Input: the provisional geometric variables $\bar{\mathbf{U}}^{n+1} = (\bar{\mathbf{X}}_i^{n+1}, \bar{V}_i^{n+1}, \bar{\kappa}_i^{n+1})$ obtained from the fully discrete scheme (4.13), the auxiliary energy variable R^n , and the time step Δt .

- **Step 1: Compute discrete Willmore energy.** Evaluate

$$W_c^{n+1}(\bar{\mathbf{U}}^{n+1}) = \frac{1}{2} \sum_{i=1}^M (\bar{\kappa}_i^{n+1})^2 |\delta_\rho \bar{\mathbf{X}}_i^{n+1}| + C.$$

- **Step 2: Compute discrete dissipation rate.**

$$D^{n+1} = \sum_{i=1}^M (\bar{V}_i^{n+1})^2 |\delta_\rho \bar{\mathbf{X}}_i^n|.$$

- **Step 3: Update the auxiliary energy variable.**

$$R^{n+1} = \frac{R^n}{1 + \Delta t D^{n+1} / W_c^{n+1}},$$

which ensures the discrete energy dissipation $R^{n+1} \leq R^n$.

- **Step 4: Compute the energy matching factor.**

$$\eta^{n+1} = \frac{R^{n+1}}{W_c^{n+1}}, \quad k_c^{n+1} = 1 - (1 - \eta^{n+1})^r,$$

where $r > 0$ is a user-chosen smoothing parameter.

- **Step 5: Energy-stabilized update.**

$$\mathbf{U}_i^{n+1} = k_c^{n+1} \bar{\mathbf{U}}_i^{n+1}, \quad i = 1, \dots, M.$$

This scaling guarantees that the updated geometric state matches the corrected energy level R^{n+1} .

- **Step 6: Prepare for the next time step.** Use \mathbf{U}^{n+1} and R^{n+1} as input for the evolution at $t = t^{n+2}$.

Output: the stabilized geometric variables \mathbf{U}^{n+1} and the updated auxiliary variable R^{n+1} .

Proof. For convenience, we denote

$$a^{n+1} := \Delta t \frac{D^{n+1}}{W_c^{n+1}} \geq 0.$$

From the Algorithm 3, R^{n+1} can be rewritten as

$$R^{n+1} = \frac{R^n}{1 + a^{n+1}}.$$

Hence, we have

$$R^{n+1} - R^n = R^n \left(\frac{1}{1 + a^{n+1}} - 1 \right) = - \frac{R^n a^{n+1}}{1 + a^{n+1}} = - a^{n+1} R^{n+1}.$$

Substituting the definition of a^{n+1} yields

$$R^{n+1} - R^n = - \Delta t \frac{R^{n+1}}{W_c^{n+1}} D^{n+1}.$$

Since $R^{n+1} > 0$, $W_c^{n+1} > 0$, and $D^{n+1} \geq 0$, the right-hand side is non-positive, implying

$$R^{n+1} \leq R^n.$$

Therefore, the energy is unconditionally stable. \square

Theorem 4.2 (Boundedness of the original energy). *Assume that \mathbf{U}^{n+1} is updated according to Step 5 of Algorithm 3, where the matching factor η^{n+1} and scaling factor k_c^{n+1} are given in Step 4. Then there exists a positive constant M_r , depending only on r and the initial auxiliary energy R^0 , such that*

$$W(\mathbf{U}^n) \leq M_r^2, \quad \forall n \geq 0.$$

Proof. From Theorem 4.1, we have demonstrated that $0 \leq R^{n+1} \leq R^n \leq \dots \leq R^0$. Without loss of generality, we assume $C \geq 1$. Hence, there holds

$$0 \leq \eta^{n+1} = \frac{R^{n+1}}{W_c^{n+1}} \leq \frac{R^0}{W_c^{n+1}} \leq \frac{R^0}{W^{n+1} + 1}.$$

Since $k_c^{n+1} = 1 - (1 - \eta^{n+1})^r$ is an r -th degree polynomial in η^{n+1} , there exists a constant $M_r > 0$, depending only on r , such that

$$|k_c^{n+1}| \leq \frac{M_r}{W^{n+1} + 1}. \quad (4.15)$$

Using the homogeneity of the discrete Willmore energy and the inequality (4.15), we have

$$W(\mathbf{U}^{n+1}) = (k_c^{n+1})^2 W(\bar{\mathbf{U}}^{n+1}) \leq \frac{M_r^2}{(W(\bar{\mathbf{U}}^{n+1}) + 1)^2} W(\bar{\mathbf{U}}^{n+1}) \leq M_r^2.$$

Therefore, the boundedness of the energy has been proven. \square

Remark 10. Motivated by the scalar auxiliary variable (SAV) methodology [39–43], we draw upon its underlying idea to develop an EC algorithm. It should be emphasized that the resulting energy used in this procedure is merely an auxiliary quantity and does not coincide with the true Willmore energy. To enforce the stability of the genuine Willmore energy, a Lagrange multiplier formulation can in principle be employed [44]. However, its theoretical applicability is restricted to BDF1 and BDF2 time discretizations. Moreover, owing to the strong nonlinearity of the Willmore equation, the resulting algebraic systems may suffer from ill-posedness or near singularity, a phenomenon that has been consistently observed in our extensive numerical experiments. These limitations motivate the incorporation of SAV-inspired concepts into the development of the proposed EC algorithm.

Remark 11. All adaptive numerical schemes considered in this paper are based on fully implicit formulations. Since iterative solvers are required, the computational cost is higher than that of linearized methods; however, in practical computations the number of iterations typically remains at a relatively low level. Moreover, due to the use of finite difference discretizations in space, the computational cost of each iteration is relatively small, and consequently the overall computational complexity is not significantly increased. We have also carried out numerical experiments using linearized methods, and the results indicate that their numerical performance is likewise satisfactory, with the advantages brought by adaptivity still being clearly observed. In view of the stability properties inherent to implicit schemes and for reasons of brevity, we do not further investigate linearized methods in this work; nevertheless, our results confirm that linearized approaches are numerically feasible.

5. Numerical experiments

In this section, we present numerical experiments for the A-WAR algorithm and the A-BDFk-FDMs, together with the EC algorithm. These experiments are conducted to evaluate their convergence properties and overall effectiveness in practical computations.

For the implementation of our numerical method, an initial configuration $(\mathbf{X}^0, V^0, \kappa^0)$ is required. To obtain a compatible starting value for the normal velocity V^0 and the mean curvature κ^0 , we begin with a smooth initial curve Γ_0 , for which both the curvature $\kappa^0 = -\mathbf{n} \cdot \partial_{ss}\mathbf{X}^0$ and the velocity $V^0 = \partial_{ss}\kappa^0 + \frac{1}{2}(\kappa^0)^3$ can be computed explicitly. These quantities are then adopted as the initial approximation $(\mathbf{X}^0, V^0, \kappa^0)$ in our iterative solver. The stopping criterion for the iteration is set to $\text{tol} = 10^{-8}$, and we select the relax time constant $\mathcal{J} = 0.5$.

Example 1 (Convergence tests). In this example, we assess the accuracy and convergence rate of the A-WAR algorithm and the A-BDFk-FDMs. The initial interface is chosen as the unit circle,

$$\mathbf{X}^0(\rho_j) = (\cos(2\pi\rho_j), \sin(2\pi\rho_j))^T, \quad 0 \leq j \leq M-1.$$

Following [30], the exact solution to the Willmore flow (2.2) is given by

$$\mathbf{X}(\rho, t) = R(t) \mathbf{X}^0(\rho), \quad V(\rho, t) = \frac{1}{2}R(t)^{-3}, \quad \kappa(\rho, t) = R(t)^{-1},$$

for $\rho \in \mathbb{T}$ and $t \geq 0$, where $R(t) = (1 + 2t)^{1/4}$. We introduce the combined geometric variable $\mathbf{U} := (\mathbf{X}, V, \kappa)$ together with its numerical approximation at $t = T$, defined by

$$\mathbf{U}_{h_\ell}^{N_\ell} := (\mathbf{X}_{h_\ell}^{N_\ell}, V_{h_\ell}^{N_\ell}, \kappa_{h_\ell}^{N_\ell}), \quad N_\ell = \frac{T}{\Delta t_\ell}.$$

The error and the associated experimental convergence order are defined by

$$e_\ell^h = \left\| \mathbf{U}_{h_\ell}^{N_\ell} - \mathbf{U}(\cdot, T) \right\|_\infty, \quad \text{order}_\ell = \frac{\log(e_\ell^h / e_{\ell+1}^h)}{\log(\Delta t_\ell / \Delta t_{\ell+1})}.$$

To facilitate the simultaneous measurement of temporal and spatial convergence rates, we impose the relation $h^2 \approx \Delta t^k$. Accordingly, the pair $(h_\ell, \Delta t_\ell)$ is updated as

$$(h_{\ell+1}, \Delta t_{\ell+1}) = \begin{cases} (h_\ell/2, \Delta t_\ell/4), & \text{BDF1}, \\ (h_\ell/2, \Delta t_\ell/2), & \text{BDF2}, \\ (h_\ell/2^{3/2}, \Delta t_\ell/2), & \text{BDF3}, \\ (h_\ell/4, \Delta t_\ell/2), & \text{BDF4}. \end{cases}$$

Figs. 5.1–5.2 present the errors obtained from the A-WAR algorithm and the A-BDFk-FDMs. In both settings, the numerical results exhibit convergence rates that agree remarkably well with the theoretical predictions $O(\Delta t^k)$, thereby confirming first- through fourth-order temporal accuracy for BDF1–BDF4. Moreover, due to the prescribed coupling between the spatial and temporal step sizes, the computations also demonstrate a second-order convergence rate in space, which is fully consistent with the expected accuracy $O(h^2)$.

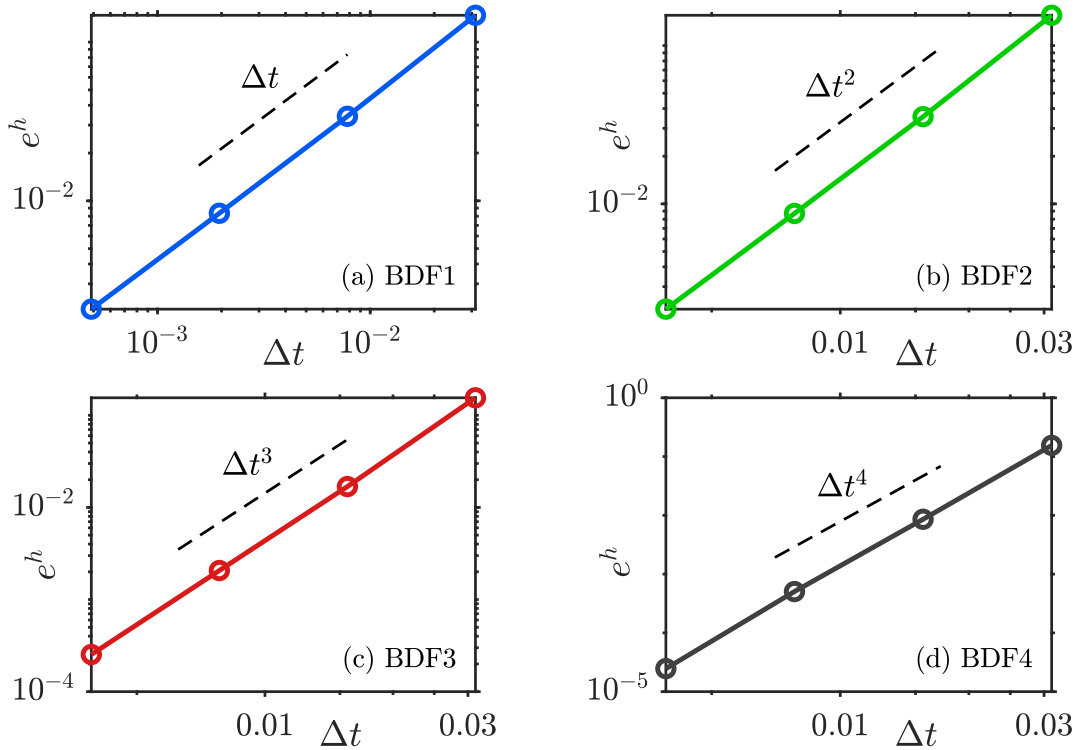


Figure 5.1: Plot of temporal errors e^h for the A-WAR algorithm using BDFk time discretizations at $T = 2$: (a) BDF1, (b) BDF2, (c) BDF3, and (d) BDF4.

Example 2. In this example, we compare the mesh distribution and mesh quality of three numerical methods, namely the BDFk-FDMs, the A-WAR algorithm, and the A-BDFk-FDMs, during the curve evolution process. For convenience, we restrict our attention to the case $k = 1$. We consider three types of initial curves and examine the corresponding grid point distributions generated by the three methods. It can be observed from Fig. 5.3, Fig. 5.5 and Fig. 5.7 that, as the geometric complexity of the initial curves increases, both adaptive methods proposed in this work are able to maintain good mesh quality throughout the evolution. This, in turn, ensures the reliability and correctness of the computed curve evolution.

In addition, to evaluate the mesh quality, several quantitative measures are employed. In particular, the ratio between the maximum and minimum arc lengths,

$$R_1(\Delta s) := \frac{\max(\Delta s)}{\min(\Delta s)},$$

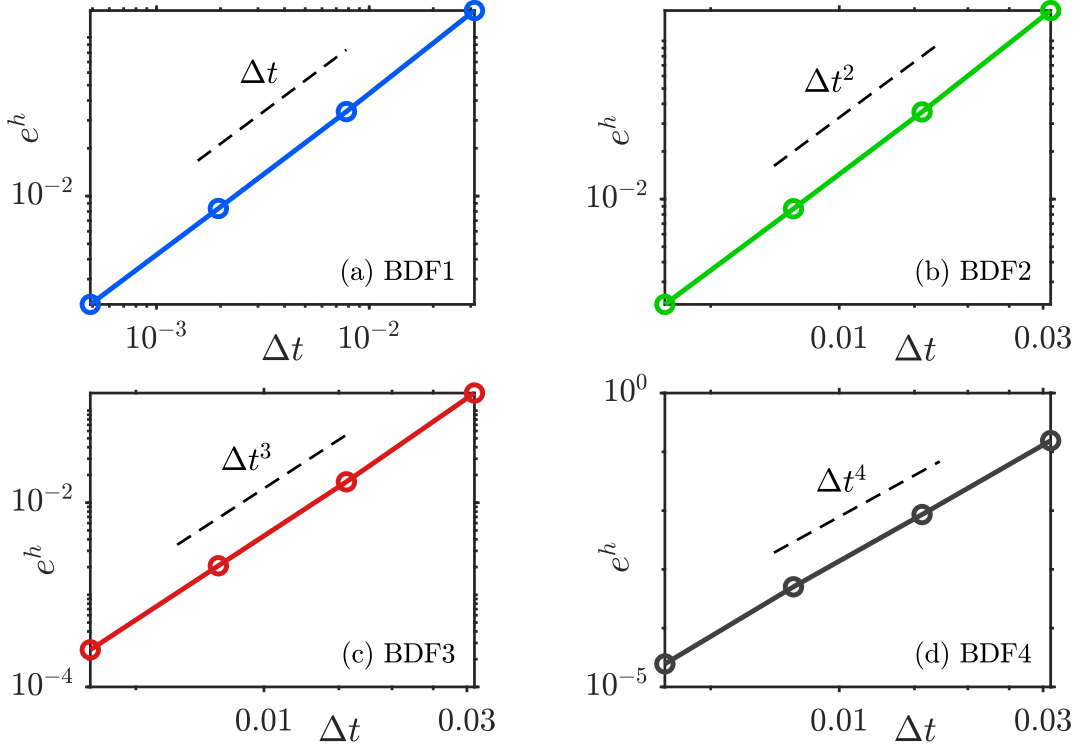


Figure 5.2: Plot of temporal errors e^h for the A-BDFk-FDM using BDFk time discretizations at $T = 2$: (a) BDF1, (b) BDF2, (c) BDF3, and (d) BDF4.

is used as a standard indicator of mesh uniformity. In addition, the mesh quality measure

$$R_2(M_f, \Delta s) := \frac{\max(M_f \Delta s)}{\min(M_f \Delta s)}$$

is adopted to assess the consistency of the mesh in the equidistribution sense induced by the monitor function M_f . As shown in Fig. 5.4, Fig. 5.6 and Fig. 5.8, the two adaptive methods proposed in this work, namely the A-WAR algorithm and the A-BDFk-FDMs, are able to rapidly form a near-equidistributed mesh at the early stage of the evolution. For both adaptive methods, the two mesh quality indicators remain close to unity throughout the entire computation, indicating good mesh uniformity and a strong adherence to the equidistribution principle induced by the monitor function.

In contrast, the BDFk-FDMs exhibit markedly different mesh evolution behaviors. As shown in Fig. 5.4, the mesh quality indicators of the BDFk-FDMs remain bounded during the evolution and gradually converge to finite constants, indicating that, for certain initial curves, the mesh maintains a certain level of overall stability. However, these limiting values are clearly larger than unity, implying that the resulting mesh does not attain an ideal mesh distribution, and its uniformity and adaptivity are significantly inferior to those of the adaptive methods. In Fig. 5.6, both mesh quality indicators deteriorate rapidly within a short time, indicating that mesh degradation severely impairs the long-time numerical computation. More critically, in Fig. 5.8, both mesh quality indicators experience a sharp growth during the intermediate stage of the evolution and later decrease to relatively small values; however, as can be observed from Fig. 5.7, the corresponding evolution curve has already become completely incorrect.

These results indicate that, for initial curves with high curvature or pronounced curvature variations, the BDFk-FDMs are prone to severe mesh distortion and strong point clustering during the evolution, which significantly undermines the reliability of the numerical solution. In some cases, such mesh degradation may even lead to a complete failure of the numerical computation. In contrast, the A-WAR algorithm and the A-BDFk-FDMs proposed in this work are able to effectively control the mesh distribution and maintain good mesh quality throughout the evolution, thereby significantly enhancing the stability and reliability of the numerical simulations.

Example 3. (Energy stability) Since the energy stability of the A-BDFk-FDMs cannot be readily established, Algorithm 3 introduces an EC strategy to address this issue. In this example, we investigate the temporal evolution of several energy-related quantities under different BDF orders. As shown in Fig. 5.9, the numerical results indicate that both the original energy W^n and the corrected energy R^n exhibit a consistent monotone decay throughout the simulation. Moreover, the ratio R^n/W^n evolves smoothly in time and remains stable during the evolution, with $R^n/W^n \approx 1$. This implies that the corrected energy R^n remains very close to the discrete energy W^n . Consequently, the proposed algorithm achieves

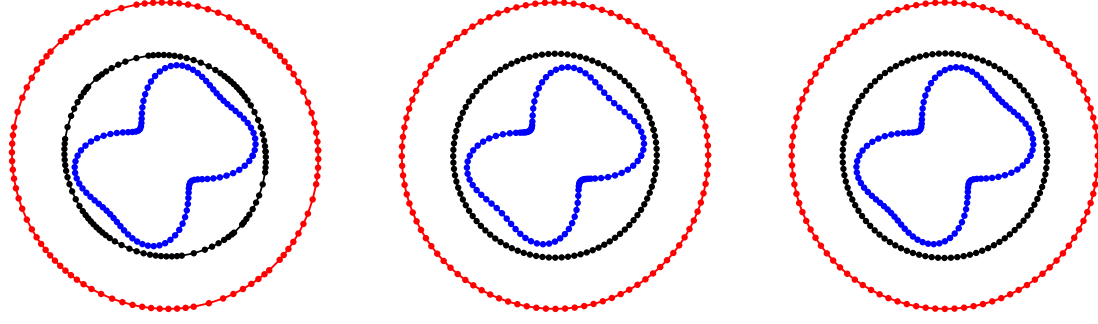


Figure 5.3: Mesh evolution computed by different numerical methods for the initial curve defined by $x = \cos(2\pi\rho)[1 + 0.3 \sin(4\pi\rho) + 0.2 \cos(8\pi\rho)]$, $y = \sin(2\pi\rho)[1 + 0.3 \sin(4\pi\rho) + 0.2 \cos(8\pi\rho)]$. From left to right, the results correspond to the BDFk-FDMs, the A-WAR algorithm, and the A-BDFk-FDMs. The blue, black, and red curves represent the configurations at $t = 0$, $t = 1.5$, and $t = 10$, respectively.

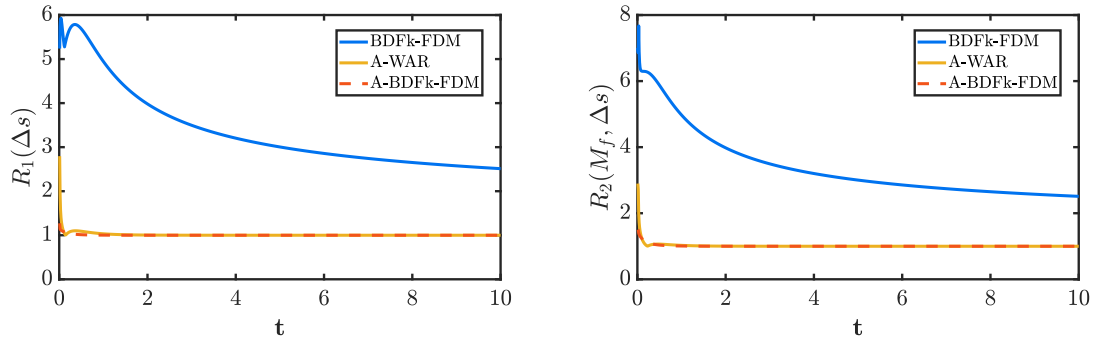


Figure 5.4: Time evolution of the mesh quality indicators $R_1(\Delta s)$ (left) and $R_2(M_f, \Delta s)$ (right) for the initial curve shown in Fig 5.3. The results correspond to the BDFk-FDMs, the A-WAR algorithm, and the A-BDFk-FDMs.

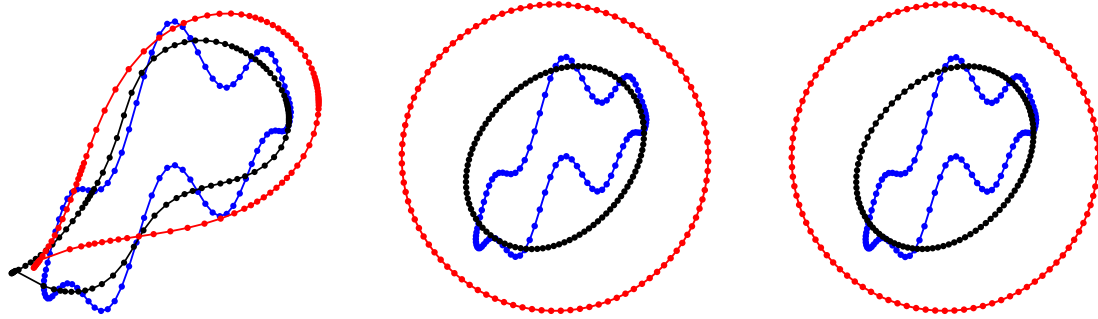


Figure 5.5: Mesh evolution computed by different numerical methods for the initial curve defined by $x = 1.2 \cos(2\pi\rho)$, $y = 0.5 \sin(2\pi\rho) + \sin(\cos(2\pi\rho)) + \sin(2\pi\rho)[0.2 + \sin(2\pi\rho)\sin^2(6\pi\rho)]$. From left to right, the results correspond to the BDFk-FDMs, the A-WAR algorithm, and the A-BDFk-FDMs. The blue, black, and red curves represent the configurations at $t = 0$, $t = 4$, and $t = 10$, respectively.

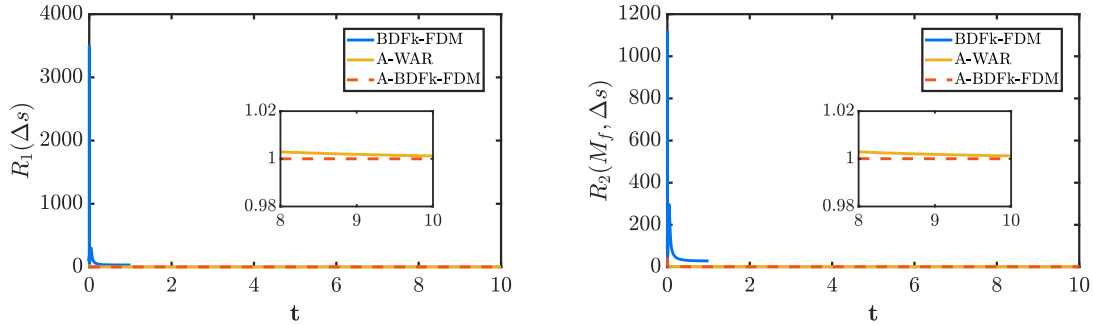


Figure 5.6: Time evolution of the mesh quality indicators $R_1(\Delta s)$ (left) and $R_2(M_f, \Delta s)$ (right) for the initial curve shown in Fig 5.5. The results correspond to the BDFk-FDMs, the A-WAR algorithm, and the A-BDFk-FDMs.

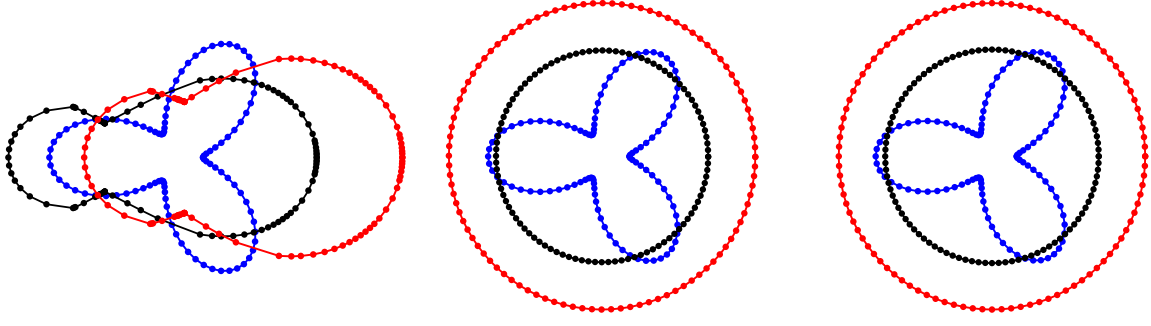


Figure 5.7: Mesh evolution computed by different numerical methods for the initial curve defined by $x = \cos(2\pi\rho)[1 - 0.65 \cos(6\pi\rho)]$, $y = \sin(2\pi\rho)[1 - 0.65 \cos(6\pi\rho)]$. From left to right, the results correspond to the BDFk-FDMs, the A-WAR algorithm, and the A-BDFk-FDMs. The blue, black, and red curves represent the configurations at $t = 0$, $t = 1.5$, and $t = 10$, respectively.

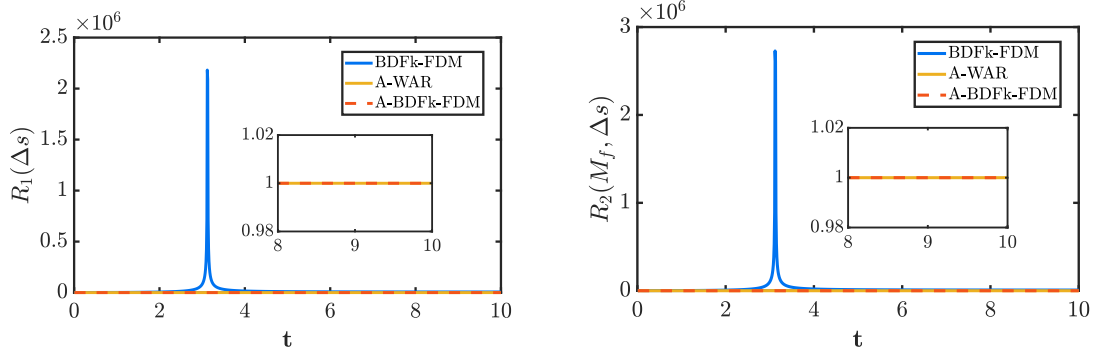


Figure 5.8: Time evolution of the mesh quality indicators $R_1(\Delta s)$ (left) and $R_2(M_f, \Delta s)$ (right) for the initial curve shown in Fig 5.7. The results correspond to the BDFk-FDMs, the A-WAR algorithm, and the A-BDFk-FDMs.

excellent energy stability both theoretically and numerically, and is applicable to arbitrary high-order time discretization schemes.

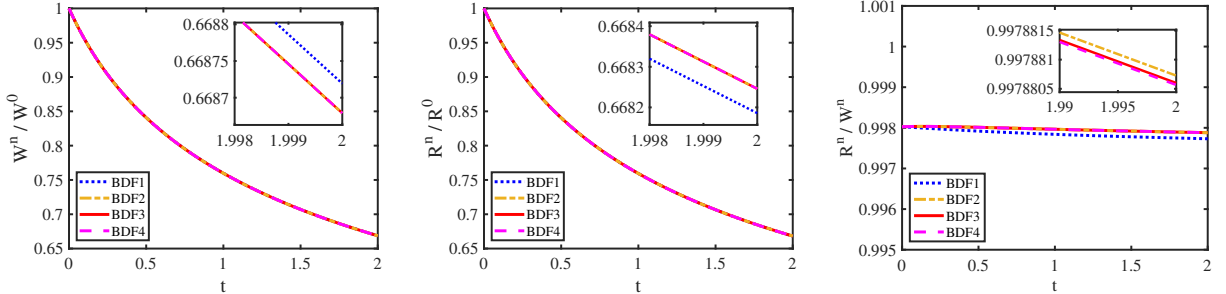


Figure 5.9: Time evolution of energy-related quantities produced by the proposed energy correction algorithm with A-BDFk-FDM for the evolution of an initial curve defined by $x = \cos(2\pi\rho)$ and $y = \sin(2\pi\rho)$. The left panel shows the normalized discrete Willmore energy W^n/W^0 , the middle panel displays the normalized corrected energy R^n/R^0 , and the right panel presents the ratio R^n/W^n . The computational parameters are $T = 2$, $\Delta t = 0.001$, and $r = 5$.

Example 4. (Evolution from simple to complex initial shapes) We present the evolution of planar curves under the Willmore flow for a sequence of test cases with increasing geometric complexity, as shown in Fig. 5.10. The initial curves range from relatively simple, nearly convex shapes to highly nonconvex configurations featuring narrow necks and pronounced geometric oscillations. For all considered initial curves, both the A-WAR algorithm and the A-BDFk-FDMs are able to compute the curve evolution over the entire time interval without numerical breakdown. As illustrated in the figure, the curves exhibit an approximately uniform expansion while their geometries become progressively smoother. Notably, even for the most intricate nonconvex initial shapes, the numerical evolution remains stable and free of spurious oscillations or loss of resolution. The incorporation of adaptivity plays a crucial role in ensuring the robustness of the numerical scheme, allowing accurate resolution of geometric features and maintaining stability throughout the entire evolution process.

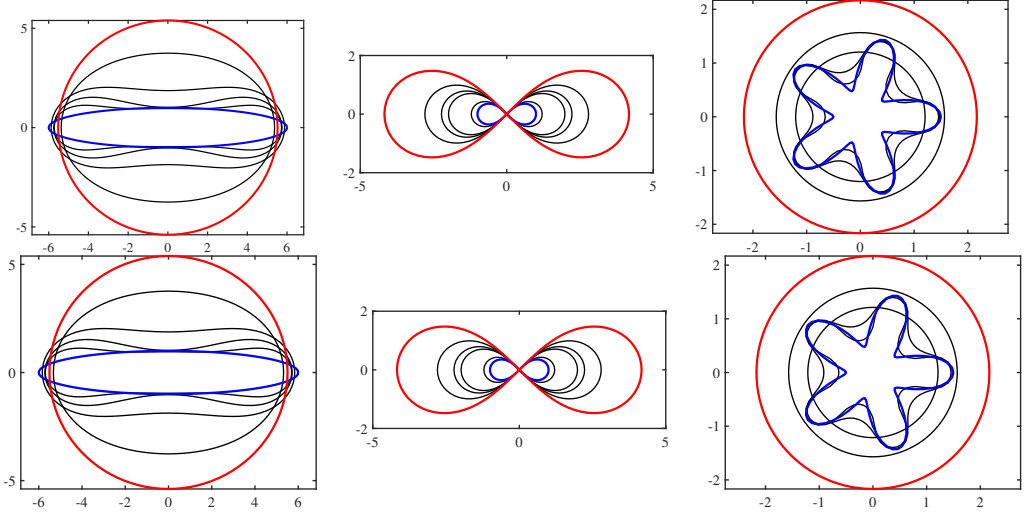


Figure 5.10: The first row corresponds to the A-WAR algorithm, while the second row shows the results obtained with the A-BDFk-FDMs ($k=1$). In each subplot, the initial curve is shown in blue, several intermediate states are plotted in black, and the final curve is displayed in red. Left column: the initial curve is given by $x(\rho) = 6 \cos(2\pi\rho)$ and $y(\rho) = \sin(2\pi\rho)$. The curves are shown at times $t = 0, 1, 5, 20, 80, 300$. Middle column: the initial curve is given by $x = \frac{\cos(2\pi\rho)}{1+\sin^2(2\pi\rho)}$, $y = \frac{\sin(2\pi\rho)}{1+\sin^2(2\pi\rho)}$. The curves are shown at times $t = 0, 0.1, 0.3, 0.6, 1.2, 10$. Right column: the initial curve is given by $x = (1 + 0.5 \cos(10\pi\rho)) \cos(2\pi\rho)$, $y = (1 + 0.5 \sin(10\pi\rho)) \sin(2\pi\rho)$. The curves are shown at times $t = 0, 0.002, 0.015, 0.05, 0.05, 2, 10$.

6. Conclusions

This study investigates adaptive FDMs for the Willmore flow from two complementary perspectives. The first approach, referred to as the A-WAR algorithm, focuses on the redistribution of discretization points through geometry-informed adaptation. The second approach, referred to as the A-BDFk-FDMs, is based on a fully adaptive moving mesh formulation. Specifically, by combining the tangential velocity equation derived from the variational derivative of a mesh functional involving the chosen monitor function and the normal velocity equation, we obtain a new total velocity formulation that leads to a fully adaptive moving mesh Willmore system. Moreover, an EC algorithm is further developed for the A-BDFk-FDMs to theoretically guarantee the energy stability of the numerical method. Both approaches are shown to be effective in maintaining mesh quality during the evolution process. Extensive numerical experiments demonstrate that the proposed methods provide reliable and efficient approximations of the Willmore flow for interfaces with nontrivial geometric features, thereby supporting their applicability to long-time simulations of curvature-driven interface evolution. In future work, we will continue to investigate adaptive numerical methods for two- and three-dimensional geometric flow problems, and further develop adaptive algorithms that preserve essential structural properties.

Appendix A. Choice of monitor function

In this appendix, we provide a geometric motivation for the form of the monitor functions used in the main text by analyzing the local interpolation error of a smooth curve approximated by a linear polygonal interpolant.

To elucidate how local geometric features of an evolving curve influence interpolation accuracy, we consider a sufficiently smooth planar curve Γ and focus on a local segment Γ_i determined by two consecutive nodes \mathbf{X}_i and \mathbf{X}_{i+1} . As illustrated in Fig. A.1, the local geometric interpolation error can be interpreted as the maximum normal deviation between the smooth curve and its linear polygonal interpolant. We denote the distance between the two consecutive nodes by $h_i = \|\mathbf{X}_{i+1} - \mathbf{X}_i\|$. Since the normal distance between a curve and its linear interpolation is invariant under rigid motions, we may, without loss of generality, apply a local translation and rotation of coordinates. Specifically, the point \mathbf{X}_i is mapped to the origin, and the direction of the linear interpolant connecting \mathbf{X}_i and \mathbf{X}_{i+1} is aligned with a reference axis. In the resulting local coordinate system, the curve segment Γ_i can be represented in graph form as $\bar{\Gamma}(\bar{x})$, $\bar{x} \in [0, h_i]$, with the normalization $\bar{\Gamma}(0) = 0$. Let $\bar{x}_* \in (0, h_i)$ denote a point at which the normal deviation between the curve and its linear interpolant attains its maximum. By the necessary condition for an extremum, we have $\bar{\Gamma}'(\bar{x}_*) = 0$.

Using the Taylor expansion of $\bar{\Gamma}(\bar{x})$ in the neighborhood of $\bar{x} = 0$ and evaluating it at $\bar{x} = \bar{x}_*$, we obtain

$$\bar{\Gamma}(\bar{x}_*) = \frac{\bar{x}_*^2}{2} \bar{\Gamma}''(\bar{x}_*) - \frac{\bar{x}_*^3}{6} \bar{\Gamma}'''(\bar{x}_*) + O(\bar{x}_*^4). \quad (\text{A.1})$$

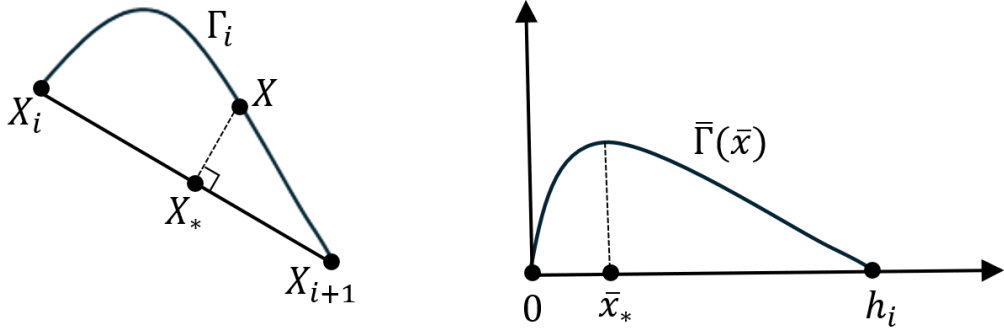


Figure A.1: Left: A local segment Γ_i of a smooth planar curve together with its piecewise linear interpolation between consecutive nodes \mathbf{X}_i and \mathbf{X}_{i+1} . For a point \mathbf{X} on the curve, the local interpolation error is measured by the normal distance to the corresponding point \mathbf{X}_* on the linear interpolant. Right: After applying a rigid translation and rotation, the curve segment is represented in graph form as $\bar{\Gamma}(\bar{x})$ over the interval $[0, h_i]$. The maximal geometric interpolation error on Γ_i corresponds to the absolute maximum of $\bar{\Gamma}(\bar{x})$, attained at $\bar{x} = \bar{x}_*$.

We first examine the contribution of the second-order term. For a planar curve expressed in graph form, the curvature is given by

$$|\kappa| = \frac{|\bar{\Gamma}''|}{\left[1 + (\bar{\Gamma}')^2\right]^{3/2}}.$$

At the point \bar{x}_* , where $\bar{\Gamma}'(\bar{x}_*) = 0$, this relation simplifies to

$$|\bar{\Gamma}''(\bar{x}_*)| = |\kappa(\bar{x}_*)|.$$

Consequently, the second-order term in the Taylor expansion contributes an error component proportional, in magnitude, to $\bar{x}_*^2|\kappa|$, indicating that in regions of mild curvature the local interpolation error is primarily curvature-driven.

We next consider the geometric interpretation of the third-order remainder term. For convenience of description, we temporarily employ the arc-length parametrization and write the curve as $\mathbf{X}(s)$. The Frenet-Serret relations for planar curves imply

$$\mathbf{X}''(s) = -\kappa(s)\mathbf{n}(s), \quad \mathbf{X}'''(s) = -\partial_s\kappa(s)\mathbf{n}(s) + \kappa^2(s)\mathbf{\tau}(s),$$

where $\mathbf{\tau}(s)$ and $\mathbf{n}(s)$ denote the unit tangent and normal vectors, respectively. It follows that the third derivative of \mathbf{X} satisfies

$$|\mathbf{X}'''(s)| \leq |\partial_s\kappa(s)| + |\kappa(s)|^2.$$

Under the assumption of locally small slopes, the third derivative $\bar{\Gamma}'''(\bar{x}_*)$ in the graph representation is of the same order as $\mathbf{X}'''(s)$ in the arc-length parametrization, and hence

$$|\bar{\Gamma}'''(\bar{x}_*)| \lesssim |\partial_s\kappa(\bar{x}_*)| + |\kappa(\bar{x}_*)|^2.$$

Substituting this estimate into the (A.1) and using $\bar{x}_* \leq h_i$, we obtain an upper bound for the local geometric interpolation error on the segment Γ_i :

$$\begin{aligned} \max_{\bar{x} \in (0, h_i)} |\bar{\Gamma}(\bar{x})| &\lesssim h_i^2 |\kappa| + h_i^3 |\partial_s\kappa| + h_i^3 |\kappa|^2 \\ &\lesssim C_1 h_i^2 |\kappa| + C_2 h_i^3 |\partial_s\kappa| + C_3 h_i^3 |\kappa|^2, \end{aligned}$$

where the constants C_1 , C_2 , and C_3 depend only on the regularity of the curve.

This estimate reveals a hierarchical structure in the local geometric interpolation error. Unlike [36], where the monitor function is constructed solely in terms of the curvature κ under an implicit asymptotic assumption $h_i \rightarrow 0$, we consider a more general and practically relevant setting in which the local mesh size h_i is not necessarily small. In this regime, different geometric contributions may enter the error expansion at comparable orders. In particular, when the term associated with curvature variation satisfies $\kappa = O(h_i\kappa_s)$, the contribution of κ_s appears at the same order and therefore cannot be neglected. Similarly, when $\kappa = O(h_i\kappa^2)$, the curvature-squared term κ^2 also contributes non-negligibly to the local error. This analysis provides a theoretical justification for incorporating higher-order geometric information into the design of monitor functions.

References

- [1] U. Seifert, Configurations of fluid membranes and vesicles, *Adv. Phys.* 46 (1997) 13–137.
- [2] W. Helfrich, Elastic properties of lipid bilayers: theory and possible experiments, *Z. Naturforsch. C* 28 (11-12) (1973) 693–703.
- [3] O.-Y. Zhong-can, W. Helfrich, Bending energy of vesicle membranes: General expressions for the first, second, and third variation of the shape energy and applications to spheres and cylinders, *Phys. Rev. A* 39 (1989) 5280–5288.
- [4] Z.-C. Ou-Yang, W. Helfrich, Bending energy of vesicle membranes: General expressions for the first, second, and third variation of the shape energy and applications to spheres, *Phys. Rev. A* 39 (1989) 5280–5288.
- [5] D. Boal, Mechanics of the cell membrane, *Eur. Phys. J. B* 15 (1998) 445–456.
- [6] U. Seifert, Configurations of fluid membranes and vesicles, *Adv. Phys.* 46 (1) (1997) 13–137.
- [7] C. V. Thompson, Solid-state dewetting of thin films, *Annu. Rev. Mater. Res.* 42 (2012) 399–434.
- [8] W. W. Mullins, Theory of thermal grooving, *J. Appl. Phys.* 28 (3) (1957) 333–339.
- [9] P. Canham, The minimum energy of bending as a possible explanation of the biconcave shape of the human red blood cell, *J. Theor. Biol.* 26 (1) (1970) 61–81.
- [10] R. Lipowsky, The conformation of membranes, *Nature* 349 (1991) 475–481.
- [11] R. Lipowsky, The morphology of lipid membranes, *Curr. Opin. Struct. Biol.* 5 (1995) 531–540.
- [12] J. W. Barrett, H. Garcke, R. Nürnberg, Parametric approximation of Willmore flow and related geometric evolution equations, *SIAM J. Sci. Comput.* 31 (1) (2008) 225–253.
- [13] G. Dziuk, E. Kuwert, R. Schatzle, Evolution of elastic curves in r^n : Existence and computation, *SIAM J. Math. Anal.* 33 (5) (2002) 1228–1245.
- [14] K. Deckelnick, G. Dziuk, C. M. Elliott, Computation of geometric partial differential equations and mean curvature flow, *Acta Numer.* 14 (2005) 139–232.
- [15] T. Willmore, *Riemannian Geometry*, Oxford University, 1993.
- [16] T. J. Willmore, *An introduction to differential geometry*, Courier Corporation, 2013.
- [17] E. Grinpun, M. Desbrun, K. Polthier, P. Schröder, A. Stern, Discrete willmore flow, *ACM Trans. Graph.* 25 (3) (2006) 1143–1151.
- [18] M. Botsch, M. Pauly, M. Gross, L. Kobbelt, Geometric modeling based on triangle meshes, *ACM SIGGRAPH Courses* (2008).
- [19] W. Welch, A. Witkin, Variational surface modeling, in: *SIGGRAPH*, 1992, pp. 157–166.
- [20] J. W. Barrett, H. Garcke, R. Nürnberg, Chapter 4 - parametric finite element approximations of curvature-driven interface evolutions, in: *Geometric Partial Differential Equations - Part I*, Vol. 21, Elsevier, 2020, pp. 275–423.
- [21] R. E. Rusu, An algorithm for the elastic flow of surfaces, *Interfaces Free Bound.* 7 (2) (2005) 229–239.
- [22] J. W. Barrett, H. Garcke, R. Nürnberg, A parametric finite element method for fourth order geometric evolution equations, *J. Comput. Phys.* 222 (1) (2007) 441–467.
- [23] B. Kovács, B. Li, C. Lubich, A convergent evolving finite element algorithm for Willmore flow of closed surfaces, *Numer. Math.* 149 (3) (2021) 595–643.
- [24] W. Bao, Y. Li, An energy-stable parametric finite element method for the planar Willmore flow, *SIAM J. Numer. Anal.* 63 (1) (2025) 103–121.
- [25] M. Li, Y. Li, Energy-stable parametric finite element methods for the generalized Willmore flow with axisymmetric geometry: Closed surfaces, *Commun. Comput. Phys.* 38 (2) (2025) 575–602.
- [26] H. Garcke, R. Nürnberg, Q. Zhao, Stable fully discrete finite element methods with BGN tangential motion for Willmore flow of planar curves, *J. Sci. Comput.* 105 (45) (2025).
- [27] E. Bänsch, P. Morin, R. H. Nochetto, A finite element method for surface diffusion: the parametric case, *J. Comput. Phys.* 203 (1) (2005) 321–343.
- [28] J. Steinhilber, Numerical analysis for harmonic maps between hypers, numerical analysis for harmonic urfaces and grid improvement for computational parametric geometric flows (2014).
- [29] J. W. Barrett, H. Garcke, R. Nürnberg, On the parametric finite element approximation of evolving hypersurfaces in \mathbb{R}^3 , *J. Comput. Phys.* 227 (9) (2008) 4281–4307.
- [30] J. W. Barrett, H. Garcke, R. Nürnberg, Parametric approximation of Willmore flow and related geometric evolution equations, *SIAM J. Sci. Comput.* 31 (1) (2008) 225–253.
- [31] C. M. Elliott, H. Fritz, On approximations of the curve shortening flow and of the mean curvature flow based on the deturck trick, *IMA J. Numer Anal* 37 (2) (2017) 543–603.
- [32] C. J. Budd, W. Huang, R. D. Russell, Adaptivity with moving grids, *Acta Numer.* 18 (2009) 111–241.
- [33] W. Huang, R. D. Russell, *Adaptive Moving Mesh Methods*, Vol. 174 of *Applied Mathematical Sciences*, Springer New York, NY, 2011.
- [34] W. Huang, Y. Ren, R. D. Russell, Moving mesh partial differential equations (MMPDES) based on the equidistribution principle, *SIAM J. Numer. Anal.* 31 (3) (1994) 709–730.

- [35] R. Li, T. Tang, P. Zhang, Moving mesh methods in multiple dimensions based on harmonic maps, *J. Comput. Phys.* 170 (2) (2001) 562–588.
- [36] J. A. Mackenzie, M. Nolan, C. F. Rowlatt, R. H. Insall, An adaptive moving mesh method for forced curve shortening flow, *SIAM J. Sci. Comput.* 41 (2) (2019) A1170–A1200.
- [37] W. Huang, J. Ma, R. D. Russell, A study of moving mesh pde methods for numerical simulation of blow-up in reaction diffusion equations, *J. Comput. Phys.* 227 (13) (2008) 6532–6552.
- [38] W. Bao, Y. Li, An energy-stable parametric finite element method for the planar Willmore flow, *SIAM J. Numer. Anal.* 63 (1) (2025) 103–121.
- [39] F. Huang, J. Shen, A new class of implicit–explicit BDFk SAV schemes for general dissipative systems and their error analysis, *Comput. Methods Appl. Mech. Eng.* 392 (2022) 114718.
- [40] F. Huang, J. Shen, Z. Yang, A highly efficient and accurate new scalar auxiliary variable approach for gradient flows, *SIAM J. Sci. Comput.* 42 (4) (2020) A2514–A2536.
- [41] J. Shen, J. Xu, J. Yang, The scalar auxiliary variable (SAV) approach for gradient flows, *J. Comput. Phys.* 353 (2018) 407–416.
- [42] J. Shen, J. Xu, J. Yang, A new class of efficient and robust energy stable schemes for gradient flows, *SIAM Rev.* 61 (3) (2019) 474–506.
- [43] Y. Guo, M. Li, Structure-preserving parametric finite element methods for anisotropic surface diffusion flow with minimal deformation formulation, *Comput. Phys. Commun.* 313 (2025) 109620.
- [44] H. Garcke, W. Jiang, C. Su, G. Zhang, Structure-preserving parametric finite element method for surface diffusion based on Lagrange multiplier approaches, *SIAM J. Sci. Comput.* 47 (3) (2025) A1983–A2011.